



# **MERIS ALGORITHM THEORETICAL BASIS DOCUMENT**

## **2-17 - PIXEL CLASSIFICATION**

Date: 30.05.2011

Issue: 5.0

***This Page is Intentionally Blank***

## Document Change Log

Issue/ Revision	Date	Comment
5.0	30.05.2011	Version corresponding to MERIS 3 <sup>rd</sup> reprocessing

***This Page is Intentionally Blank***

# TABLE OF CONTENTS

<b>1. INTRODUCTION .....</b>	<b>8</b>
1.1 MERIS Flags .....	8
1.2 Objectives .....	8
<b>2. ALGORITHM OVERVIEW.....</b>	<b>10</b>
2.1 The Challenge of Cloud Classification .....	10
2.2 Theoretical Description .....	13
2.2.1 Land – Water Classification .....	13
2.2.2 Cloud Screening .....	15
2.2.3 Sea Ice .....	25
2.2.4 High glint.....	25
2.2.5 Clouds Over Land.....	25
2.2.6 Snow and Ice Detection.....	28
2.3 Practical Considerations .....	30
2.3.1 Land – Water Classification.....	30
2.3.2 Cloud Screening .....	30
2.3.3 Comparison of pressure computations over land using tie-point DEM and GETASSE DEM.....	31
<b>3. ERROR BUDGET ESTIMATES.....</b>	<b>39</b>
<b>4. ASSUMPTIONS AND LIMITATIONS .....</b>	<b>40</b>
<b>5. REFERENCES .....</b>	<b>41</b>

## INDEX OF TABLES

Table 1: Estimation of adjacency effects for inland waters at 665 nm and 865 nm; results shown are TOA reflectances (%); reflectance used for water is 0.02 and 0.005 at 665 and 865 nm; reflectance for the environment is 0.1 and 0.3 respectively; R is the radius used to take adjacency effects into account.	14
Table 2: List of scenes used for the Pscatt threshold determination	24

## INDEX OF FIGURES

<i>Figure 1: Land (green) and water (black) classification of an intertidal flat (North Sea coast of Germany). Left: Level 1b classification, based on a static map. The Wadden Sea area, which is dry fallen in this image, is erroneously classified as water. Right: classification using the L2 radiometry based classification; the dry fallen areas are correctly identified</i>	14
<i>Figure 2: Examples of spectra for glitter and coarse and fine grain snow (snow1 and snow 2 respectively); wind speed is 5 m/s, solar zenith angle is 40°.</i>	16

Figure 3: <i>Geometrical constrains implied by MERIS viewing geometry and solar zenith angle as a function of Latitude, for equinox (--) and solstice (—).</i>	16
Figure 4: <i>The O2 transmittance versus the apparent pressure for 4 air masses m.</i>	18
Figure 5: Example for ambiguity of Pscatt in the case of a thick cloud, where the single scattering approximation is not valid. The Pscatt value of the cloud south of Norway is below the value of the surrounding water.	22
Figure 6: Schematic scetch of the Pscatt threshold determination	23
Figure 7: Result of the Pscatt threshold determination study.	24
Figure 8: Example of the P1 pressure product.	26
Figure 11: Subset of Orbit 21934, 11.05.2006, including part of the Alpes and of the flat pre-Alpes. The AATSR NDSI has been calculated for the whole area, and those pixels which are flagged by the MDSI (blue).	29
Figure 12: AATSR-NDSI for all pixel of the area shown in Figure 11 (blue), and for those pixels which are flagged as snow by the MDSI test (yellow). The ratio $NDSI\_MDSI / NDSI\_ALL$ is shown as red line.	29
Figure 9: Visual comparison of GETASSE 30 and tie-point DEM	32
Figure 10: hPa for the elevation of each pixel: left: DEM GETASSE; right: DEM TiePoints	36
Figure 11: difference of both dem-pressure images	36
Figure 12: Influence of GETASSE and Tiepoint DEM on the cloud identification: blue: snow; yellow: cloud_flag derived from getasse30, red: additional pixels classified as cloud using the tie_point DEM; product: 16.11.2005	37
Figure 13: Influence of GETASSE and Tiepoint DEM on the cloud identification: blue: snow; yellow: cloud_flag derived from getasse30, red: additional pixels classified as cloud using the tie_point DEM; product: 19.11.2005	38
Figure 4-1: Classification structure	39

***This Page is Intentionally Blank***

# 1. INTRODUCTION

## 1.1 MERIS Flags

The MERIS Level 2 product includes a number of so called flags, which are binary values identifying if a certain characteristic of a pixel is true or not. There are three types of these flags:

- 1) Surface types flags (land, water, cloud)
- 2) Product confidence flags (PCD)
- 3) Science flags

This ATBD describes the algorithms to derive the first set of flags, the surface type flags. The other types are described as part of relevant ATBDs, or in own ATBDs.

While the information about a pixel located over water or land can be taken from a static map as a good first guess -provided the geo-location is better than the size of the pixel-, the cloud coverage is spatially and temporally highly variable and needs to be derived from the measurement itself. After knowing whether a pixel is cloudy or clear, in the clear sky case the land-water information can be refined. This is particularly necessary in the coastal zone where the actual land-water boundary is constantly changing due to tides, whether the pixel size is small enough to resolve this difference.

## 1.2 Objectives

The Pixel Classification of MERIS data is the first part of the Level 1 to Level 2 processing. Every pixel is uniquely identified as one of the three surface types Land – Water – Cloud. This is required for the further processing, where the derived products depend on the result of this classification. For example, if a pixel is over land the vegetation indices are calculated whereas over clouds the cloud albedo is retrieved. In some cases the same products are derived for multiple surface types: for example surface pressure is derived over clouds (cloud top pressure) as well as over land (land surface pressure); a second example is aerosols which are derived over the ocean and over land. Finally water vapour is derived over all surfaces. However, also in these cases the surface type classification is important because the retrieval algorithms differ with the surface type.

In summary, the objective of the Pixel Identification for MERIS Level 2 processing is to identify and label MERIS measurements as one of the three surface types:



- Clear land
- Clear water
- Cloud

The assignment has to be unique and complete for any pixel. A surface type „unknown“ is not allowed in order to permit further processing.

Additional attributes shall be given to further qualify the surface type, if necessary. In particular, snow or ice coverage should be identified and provided to the further processing algorithms.

## 2. ALGORITHM OVERVIEW

### 2.1 The Challenge of Cloud Classification

A large portion of the earth surface is covered by clouds (Paperin et al, 2007). Consequently most earth observation images in the visible spectral domain include a significant amount of cloudy pixels. Such measurements are treated in two opposite ways: either cloud properties are retrieved, e.g. for weather forecast or climate studies (Wylie, D., 1998, Russow et al, 1999; Liou, 1992), or the focus of the interest is the earth surface – being it land or water – which is then masked by the cloud (Luo,2008). In the latter case the presence of the cloud needs to be identified, and the change of the surface reflectance due to the cloud has to be estimated.

An image pixel can be cloud free, totally cloudy, or partly cloudy:

- In the cloud free case there are no water droplets or ice crystals in the atmosphere which change the surface reflectance.
- In the totally cloudy case the optical thickness is so high that the portion of surface reflectance at the signal measured by the satellite is negligible.
- The partly cloudy case comprises all intermediate situations where the measured reflectance is a mixture of a significant portion of the surface reflectance, but modified due to the presence of a cloud. This can be either due to an optically thin cloud, or the cloud is covering only a fraction of a pixel in the field of view of the sensor (Preusker et al, 2006).

Cloud free and totally cloudy pixels can be identified rather easily, and most of the tests used in earth observation processing systems for cloud identification today, assign either of these two stages, and hence also partly cloudy cases have to be assigned to either of these two classes (Eumetsat, 2006). For spatial high resolution instruments such a binary cloud flag is not appropriate if several different higher level processing algorithms are applied, each of which having a different robustness to partial cloudy pixel (Brockmann, 2008). Some novel algorithms therefore deliver a graduated scale, as an indicator of the extend to which a signal is influenced by the presence of clouds (Schiller et al, 2008, Gomez-Chova et al, 2007, Merchant et al, 2006). Such an indicator can be related to cloud properties, e.g. apparent cloud optical thickness, the atmospheric transmission or cloud features. In MERIS 3<sup>rd</sup> reprocessing a binary flag is applied, however, the migration to a graduated scale is under discussion.

Clouds have certain characteristics which can be used for their identification and characterisation (Luo et al, 2008):

- Brightness
- Whiteness
- Cold temperature
- High altitude

However, none of these characteristics is always given if a pixel is cloudy; this is the main problem of cloud identification. For instance, thin lower clouds are difficult to differentiate from bright surfaces (like glint over water). Then other methods not based on the features given above must be used. In particular, the clouds can be also detected using the spatial and temporal variability of the reflected radiation. In addition, clouds screen the tropospheric gases. This leads to the increase in the reflection inside corresponding gaseous absorption bands (e.g., band 11 on MERIS (0.761  $\mu\text{m}$ )), which is routinely used for the cloud top height monitoring (Fischer et al., 2000a).

One way to detect clouds would be to work directly with optical measurements. Further, derived cloud physical properties can be used to characterise clouds and assess their impact on the retrieved signal. This includes, amongst others, cloud fraction, cloud top temperature, cloud top pressure, cloud type, cloud phase, cloud optical depths and cloud effective particle size. Such properties can be studied using the radiative transfer modelling. Fischer and Preusker (2000a,b) have done extensive work in this respect over the past years (see also Mullet et al, 2007, Rathke et al, 2002, Brenguier et al 2000, Pawlowska et al, 2000). They have developed the MERIS algorithms for cloud top pressure, cloud optical thickness, cloud albedo and cloud type retrieval and have translated this knowledge into a probability based cloud detection algorithm (Preusker et al, 2006).

Cloud detection became important with the systematic processing of the NOAA AVHRR instrument in the 1980s. Statistical histogram analysis methods were developed by Phulpin et al (1983). Most common used were threshold algorithms, e.g., Saunders et al. (1988). Large scale textures were identified using pattern recognition techniques as proposed by (Garant and Weinman, 1986). These methods worked quite well over the ocean but exposed problems in polar regions (separation of clouds from ice and snow) and in the tropics (low level, warm clouds). A good overview of the cloud screening

techniques at the late 80s is given by Goodman et al. (1988). Improved methods are proposed for the AVHRR (Simpson et al, 1996) and later for ATSR (Simpson et al 1998).

The cloud screening algorithms for the ATSR 1 and 2 in the 1990s were mainly based on previous work for AVHRR and use spectral threshold tests (Birks et al, 2007). The thermal band at  $12\mu\text{m}$  is used as main tool to identify the cold cloud surface by a threshold, supported by other thresholds on band differences and on the histogram of the radiance distribution in the image. The unique feature of two views under different angles of the same pixel and the spatial coherence of the radiance are also exploited. The cloud screening of the AATSR is basically the same with refined and additional tests due to additional bands. Recently, tests on vegetation and snow indices have been introduced (Birks et al, 2007). However, application oriented projects are not satisfied with the standard cloud screening and are proposing alternative methods, for example for the GlobCarbon processing (Plummer et al, 2008).

The MERIS Level 2 cloud screening up to the second reprocessing is a combination of up to 8 different tests (Santer et al, 1997). Three of those are classical threshold tests on spectral radiances or differences, and five are connected with the pressure estimates derived from the differential oxygen A-band absorption measurements. However, practically only three of tests were finally used. The potential of the O2A feature has been addressed recently in ESA funded projects, namely "Exploitation of the oxygen absorption band" and "MERIS AATSR Synergy". The result of these activities has lead to an upgrade of the operational MERIS pixel classification in the third reprocessing (this document).

The strong water vapour absorption at  $1.38\mu\text{m}$  can be used to detect the presence of high clouds, including thin cirrus under daytime viewing conditions. With sufficient atmospheric water vapour in the beam path, almost no upwelling reflected radiance from the earth's surface reaches the satellite which is in particular handy for snow covered surfaces. However, precipitable water is often less than 1 cm over polar and in high elevation regions. The  $1.38\mu\text{m}$  reflectance threshold is set to 0.03 for MODIS (Ackerman et al 2006). Unfortunately, such a band is not available in MERIS.

A big problem is the distinction between clouds and snow/ice, in particular for instruments which do not have spectral bands in the NIR and SWIR. An extensive study including the cloud screening over snow and ice has been undertaken by Stamnes, Hori and Aoki for the purpose of snow property retrieval (Aoki et al, 2007; Hori et al, 2007; Stamnes et al, 2007). Snow and ice are less reflective in the NIR spectral region, and the so called normalized differentiation ice index (NDII) and the corresponding snow index (NDSI) is a good tool to differentiate clouds from snow and ice. The reflectance for ice decreases with the wavelength much faster as compared to snow. Therefore, large values of NDII signify

the bare ice case. However, the effect of increasing absorption becomes notable for wavelengths larger than 900nm. The NDSI and NDII are using bands at 1.05 $\mu$ m and 1.64 $\mu$ m (for MODIS). MERIS bands are not optimal in this respect.

Also measurements of trace gas vertical columns (e.g., SCIAMACHY onboard ENVISAT) are disturbed by cloud presence because corresponding instruments have large fields of view to enhance the sensitivity to small gaseous concentrations. Cloud clearing algorithms are described in (Cervino et al, 2000) for GOME, and Kokhanosky has recently reported on using MERIS to support the cloud screening for SCIAMACHY (Kokhanovsky et al, 2008).

## 2.2 Theoretical Description

### 2.2.1 Land – Water Classification

Water is generally darker than land surfaces. The strong absorption of water emphasizes its darkness in the near-infrared. On the other hand, land surfaces are generally brighter in the near-infrared. The so-called adjacency effect leads to increased scattering in the atmosphere from the neighbouring land surfaces. This effect is strongest in the near-infrared. A decision has to be taken where the optimal spectral channel is located in order to get a maximum contrast between water and land, and not to be influenced strongly by the adjacency effect.

The second feature exploited to discriminate land and water is the spectral slope: whereas the spectrum of water surfaces continuously decrease for wavelength larger than 600nm (in most cases even before), vegetated land spectra have a strong increase from red to near-infrared, the so called red-edge. The steep increase is located at around 700nm.

We used a SPOT scene acquired on June 25, 1991 over SE France to set up averaged reflectances above land around 0.1 and 0.3 at 665 and 865 nm respectively. For water, we consider quite turbid water with a sediment loading of 40 mg/l which leads to respective reflectances of 0.02 and 0.005. The runs were first performed with 5S and a continental aerosol for a visibility of 23 km then for marine aerosol. The solar zenith angle was 60° for a nadir view.

We first want to apply a radiometric threshold at 670 nm or 865 nm. The adjacency effect is less pronounced at 670 nm than at 865 nm. At first glance, it appears easier to set a threshold at 670 nm than at 865 nm because this threshold value is less subject to adjacency effect. The final recommendation is to use MERIS band 6 at 670nm with a threshold which corresponds to a maximum expected water reflectance for turbid water.

This threshold should depend on sun and viewing geometry in order to take atmospheric scattering into account. A typical coastal atmosphere should be used to calculate the top of atmosphere signal.

R (km)	continental aerosols		maritime aerosols	
	665 nm	865 nm	665 nm	865 nm
0.5	5.9	4.0	5.9	5.5
1.0	5.8	3.6	5.7	4.7
2.0	5.6	3.2	5.5	4.0
5.0	5.5	2.9	5.3	3.3
10.0	5.4	2.6	5.1	2.9
20.0	5.3	2.5	5.1	2.6

**Table 1: Estimation of adjacency effects for inland waters at 665 nm and 865 nm; results shown are TOA reflectances (%); reflectance used for water is 0.02 and 0.005 at 665 and 865 nm; reflectance for the environment is 0.1 and 0.3 respectively; R is the radius used to take adjacency effects into account.**

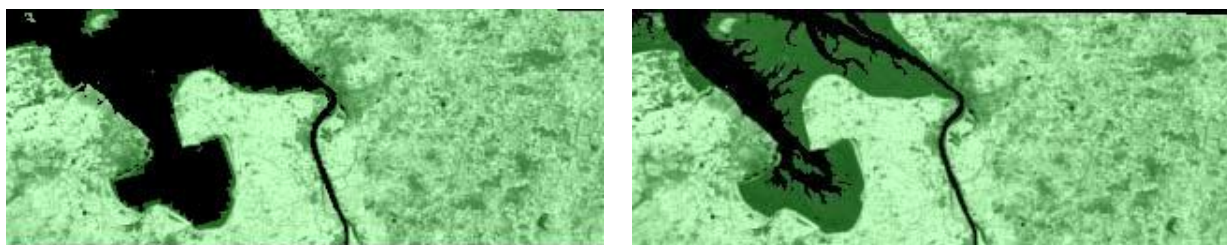


*Figure 1: Land (green) and water (black) classification of an intertidal flat (North Sea coast of Germany). Left: Level 1b classification, based on a static map. The Wadden Sea area, which is dry fallen in this image, is erroneously classified as water. Right: classification using the L2 radiometry based classification; the dry fallen areas are correctly identified*

A second test relies on the spectral dependency, with  $\rho_{665} > \rho_{865}$  for water. We can see on Table 1 that, despite strong environment effects, TOAR at 865 nm remains lower than TOAR at 665 nm.

In presence of sunglint, the above statement is no longer valid. The Fresnel reflection is white but, because of the stronger atmospheric attenuation at 670 nm than at 865 nm, the apparent contribution of the sunglint is higher at 870 nm than at 670 nm. It is there better to use the measurement at 670nm in case on medium sun glint conditions. If the sun glint becomes too high, it is no longer possible to use the radiometric measurements of a signal pixel in order to distinguish between a cloud and sun glint. In such cases it is better to test on potential high sun glint (L1b land-water flag, geometry, wind) and keep the L1b classification instead of switching to a radiometric test.

## 2.2.2 Cloud Screening

### 2.2.2.1 Clouds over ocean

The detection of clouds over the ocean appears a rather simple task: clouds are bright, and the ocean is dark. Beside this simple case, which covers most of the cloudy pixels in MERIS images, there are more difficult cases: less bright clouds, in particular thin cirrus, and bright water pixels, e.g. in coastal zone with high suspended sediments, or in the ocean with coccolithophides. Unfortunately, these cases cause a lot of problems in ocean colour remote sensing.

Even the simple case of bright clouds and dark water requires careful treatment. Different targets appear bright over the ocean: not only clouds, but also sunglint and sea ice. Outside the sun glint area bright target over the ocean can be detected using a threshold on the reflectance in a short wavelength band. Two different tests have been developed; one using tabulated values for the maximum reflectance at 442nm over oceanic waters depending on the sun and observation geometry. A second test is using a single global threshold on the Rayleigh reflected reflectance at a blue band.

The main problem then is to distinguish clouds from sea ice, outside and inside the sunglint. The spectral dependence of the clouds in the MERIS spectral domain is quite white. The Fresnel reflection is almost white, while, in most cases, the ice/snow reflectance decreases towards the infrared (Figure 2).

In any case, confusion between glitter and ice should occur for a very limited number of cases due to constraints from MERIS viewing geometry ( $\sim 40^\circ$ ) versus solar zenith angle at latitudes where ice can occur. As shown on Figure 3, geometrical conditions required to have both glitter and ice at Equinox implies that ice has to be present down to latitude of  $50^\circ$  and  $70^\circ$  for Solstice. The probability to encounter ice at these latitudes is rather low except eventually in the Southern Hemisphere.

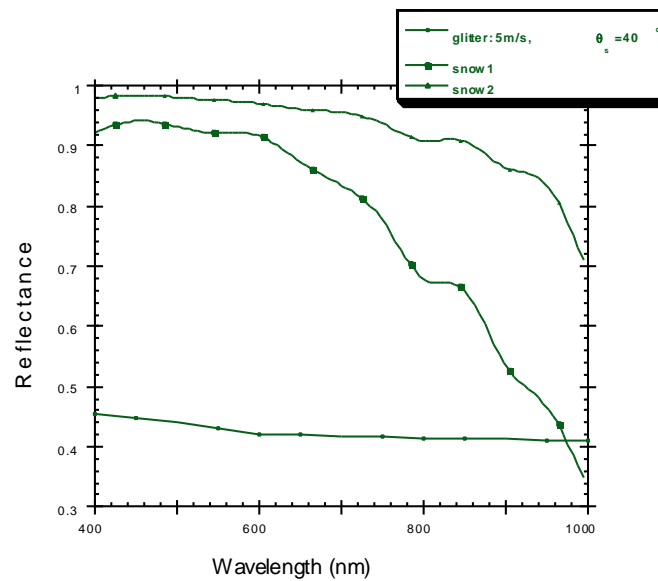


**Figure 2: Examples of spectra for glitter and coarse and fine grain snow (snow1 and snow2 respectively); wind speed is 5 m/s, solar zenith angle is 40°.**

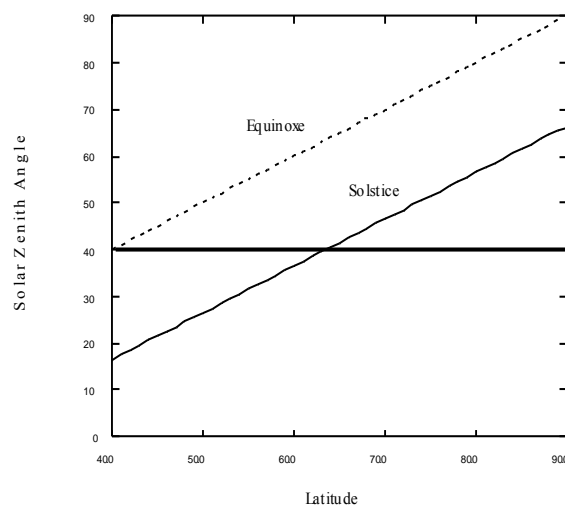


**Figure 3: Geometrical constraints implied by MERIS viewing geometry and solar zenith angle as a function of Latitude, for equinox (--) and solstice (—).**

#### 2.2.2.2 Height of the scattering surface (ocean)

Complementing the bright tests over the ocean discussed above, the altitude of the scattering surface is used. MERIS measurement in the oxygen absorption band 11 depends on the number of oxygen molecules between the sensor and the scattering surface, and hence it carries information about the height of this scattering surface. In the



case of optically thin clouds only part of the photons are scattered by the clouds; the other part reaches the surface. Hence the measurement in band 11 is a mixture of photons scattered from different heights, and when the measurements is converted into a height values this is a weighted average between the cloud and the surface; we call it the apparent height of the scatterer (Pscatt). Although it is not the real height of the (thin) cloud, it can be used to detect the cloud.

#### 2.2.2.2.1 Apparent pressure retrieval

This O2 apparent transmittance is defined as the band 11/ band 10 ratio of the TOA reflectance:

$$T_{O_2}^* = \rho_{11}^* / \rho_{ref}^* \quad (1)$$

In the reference band, we should measure the same than in B11 but without O2 absorption.

Over water,  $\rho_{ref}^*$  combines the TOA reflectance at 753 nm and 778 nm in a linear interpolation in wavelength.

The apparent pressure is defined as the pressure, which corresponds to  $T_{O_2}^*$ . We imagine a surface at a pressure level P. For a given geometry,  $T_{O_2}^*$  is the transmittance on the direct to direct path (sun-surface-satellite). For this geometry (solar zenith angle SZA and view zenith angle VZA) and an atmospheric model (P-T profile), exists a unique correspondence between  $T_{O_2}^*$  and P as illustrated in Figure 4. When  $T_{O_2}^*$  decreases, P increases continuously. The retrieval of P is straightforward:

- (i) Identify the two pressure levels P1 and P2 to bracket  $T_{O_2}^*$  MERIS.
- (ii) Apply a linear interpolation in ln(P) between P<sub>1</sub> and P<sub>2</sub>.

To account for the smile effect:

- (i) For each detector, we know the central wavelength in B11.
- (ii) LUTs of  $T_{O_2}^*$  are generated for 21 B11 MERIS filters.
- (iii)  $T_{O_2}^*$  is computed at 21 pressure levels.

- (iv) For each filter, we computed  $T_{O_2}^*$  for 24 SZA and for 24 VZA corresponding to 24 Gaussian angles.

This “surface” transmittance is computed for 21 filters, 21 pressure levels, 24 SZA, 24 VZA.

The initial pressure (ocean+ atmosphere) is  $P_1$ .

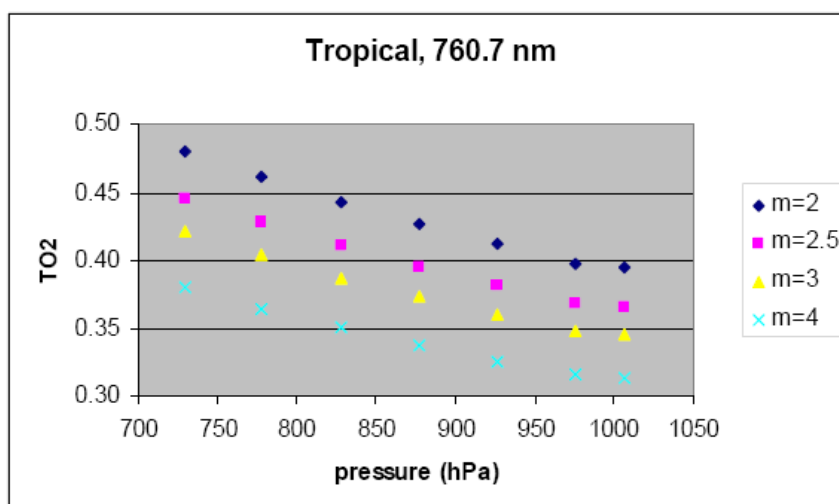


**Figure 4: The O2 transmittance versus the apparent pressure for 4 air masses  $m$ .**

#### 2.2.2.2.2 Rayleigh corrected apparent pressure

In the NIR, over the ocean, a simple but accurate correction of the coupling between molecular scattering and Fresnel reflection is used for the reference band:

$$\rho_R^{ref} = \rho_R^L (1 + R(\theta_s) + R(\theta_v)) \quad (2)$$

#### Computation of the molecular contribution in the reference band

The surface is black and the atmosphere purely molecular. The Rayleigh optical thickness is 0.025. We have a primary scattering regime. An elementary layer contributes to the TOA signal proportionally to:

- (i) The amount of molecules:  $dP$
- (ii) The O2 transmittance  $T_{O_2}(\mu_s, \mu_v, P)$

After integration on the atmospheric column, we get:

$$\rho_R^{O_2} = T_{O_2}^R \rho_R^{ref} \quad (3)$$

with:

$$T_{O_2}^R = \frac{1}{P_s} \int_0^{P_s} T_{O_2}(\mu_s, \mu_v, P) \cdot dP \quad (4)$$

as the integration of the O<sub>2</sub> transmittance over the atmospheric column.

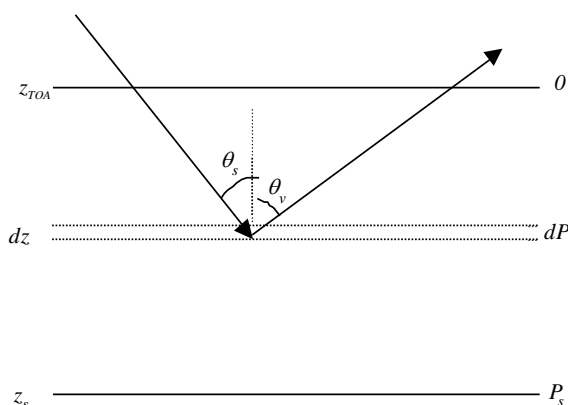


**Figure 2:** schematic representation of the atmosphere

### Rayleigh correction on the O<sub>2</sub> transmittance

The molecular contribution is known; therefore it is relevant to subtract it and to define the O<sub>2</sub> transmittance of the aerosol with:

$$T_{O_2}^a = (\rho_{11}^* - T_{O_2}^R \rho_{ref}^R) / (\rho_{ref}^* - \rho_{ref}^R) \quad (5)$$

and to associate the apparent pressure  $P_2$  of the aerosols.

### Fresnel corrected apparent pressure

The above apparent pressure of the aerosols corresponds to a black surface. If the water body is black at 761 nm, it remains the Fresnel reflection. We suppose that the direct sunglint is negligible. It remains the coupling between atmospheric scattering and Fresnel reflection. The coupling Rayleigh-Fresnel is negligible because of the small Rayleigh

optical thickness. Even if the coupling aerosol scattering and Fresnel reflection is by one order of magnitude less than the intrinsic aerosol radiance we want to introduce it.

### Modelisation

We have to consider the coupling between scattering and Fresnel reflection.

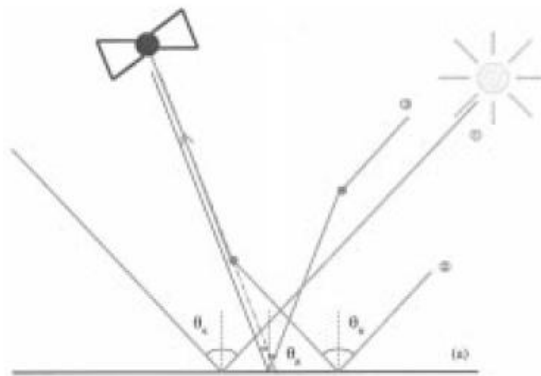


**Figure 3:** The Fresnel reflection terms

In the reference band, or in any band not affected by the gaseous absorption, we have:

$$\rho_a = \rho_a^0 + \rho_{aG} + \rho_{Ga} \quad (6)$$

$\rho_a^0$  is the aerosol reflectance over a black target (see §3).  $\rho_{aG}$  and  $\rho_{Ga}$  respectively correspond to the coupling scattering-reflection and reflection-scattering.

A simplified formulation of the signal in the reference band is:

$$\rho_{ref}^a = \rho_a^0 * (1 + (r(\theta_s) + r(\theta_v)) P_a(\chi) / P_a(\Theta)) \quad (7)$$

$1 + (r(\theta_s) + r(\theta_v)) P_a(\chi) / P_a(\Theta)$  informs on the Fresnel contribution and will be input for the possible implementation of a sunglint flag.

In which  $r(\theta_s)$  and  $r(\theta_v)$  are the Fresnel reflection coefficients.  $P_a(\chi) / P_a(\Theta)$  is the ratio of the aerosol phase functions between the forward down welling scattering at the surface and the backscattering towards the space.

For the O2 band, we have:

$$\rho_{O_2}^a = T_{O_2}^a \cdot \rho_a^0 + T_{O_2}^{aG} \cdot \rho_{aG} + T_{O_2}^{Ga} \cdot \rho_{Ga} \quad (8)$$

$T_{O_2}^{aG}$  and  $T_{O_2}^{Ga}$  are the O2 transmittances respectively on the diffuse to direct path and on the direct to diffuse path. They depend upon  $(\theta_s, \theta_v)$  and are integrated on the

atmospheric column. At each pressure level, the O2 transmittance  $T_{O_2}(\mu_s, \mu_v, P)$  is weighted by the aerosol scattering coefficient. The second dependence is on the aerosol vertical distribution, through the aerosol scale height  $H_a$ .

In the primary scattering approximation, Eq. (8) becomes:

$$\rho_a^a = \rho_a^0 ({}^0T_{O_2}^a + (T_{O_2}^{aG} \cdot r(\theta_s) + T_{O_2}^{Ga} \cdot r(\theta_v)) Pa(\chi) / Pa(\Theta)) \quad (9)$$

${}^0T_{O_2}^a$  is the O2 transmittance for the aerosols over a black surface.

By identification of Eqs. (7) and (9), we introduce an O2 transmittance for the aerosol-mirror system as:

$$T_{O_2}^a = ({}^0T_{O_2}^a + (T_{O_2}^{aG} \cdot r(\theta_s) + T_{O_2}^{Ga} \cdot r(\theta_v)) Pa(\chi) / Pa(\Theta)) / (1 + (r(\theta_s) + r(\theta_v)) Pa(\chi) / Pa(\Theta)) \quad (10)$$

#### Correct the MERIS O2 aerosol transmittance

MERIS  $T_{O_2}^a$  of Eq.(5) needs to be corrected from the coupling by a multiplicative factor  $f$ :

$$f = {}^0T_{O_2}^a / T_{O_2}^a \quad (11)$$

$f$  is greater than 1 which increases the O2 transmittance and decreases the apparent pressure of the aerosols.

The Fresnel coefficients are pre computed by degree between 0 and 90. The aerosol phase function is computed by degree between 0 and 180.

$T_{O_2}^{aG}$  and  $T_{O_2}^{Ga}$  are symmetrical. One LUT is generated for 21 filters, 24 SZA, 24 VZA.

The nominal case corresponds to:

- (i) An aerosol scale height  $H_a=2$  km.
- (ii) A power law for the size distribution with  $\alpha=-0.4$

#### 2.2.2.2.3 Limitation of Pscatt

Pscatt is derived under the single scattering approximation. This is not valid in the case of thick clouds and the values retrieved by the algorithms are misleading (see Figure 5).

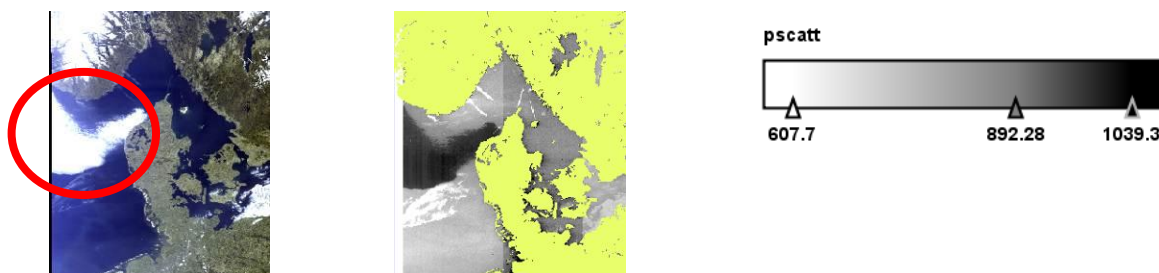


**Figure 5: Example for ambiguity of Pscatt in the case of a thick cloud, where the single scattering approximation is not valid. The Pscatt value of the cloud south of Norway is below the value of the surrounding water.**

By inspecting several products, it was found that

- Pscatt values below a certain value (around 700 hPa) are always due to clouds, often due to a thin cirrus cloud.
- Pscatt values above that value could be due to a cloud but also due to a certain ocean – aerosol combination; there are thick clouds which Pscatt value can even be below the value of the surrounding waters.

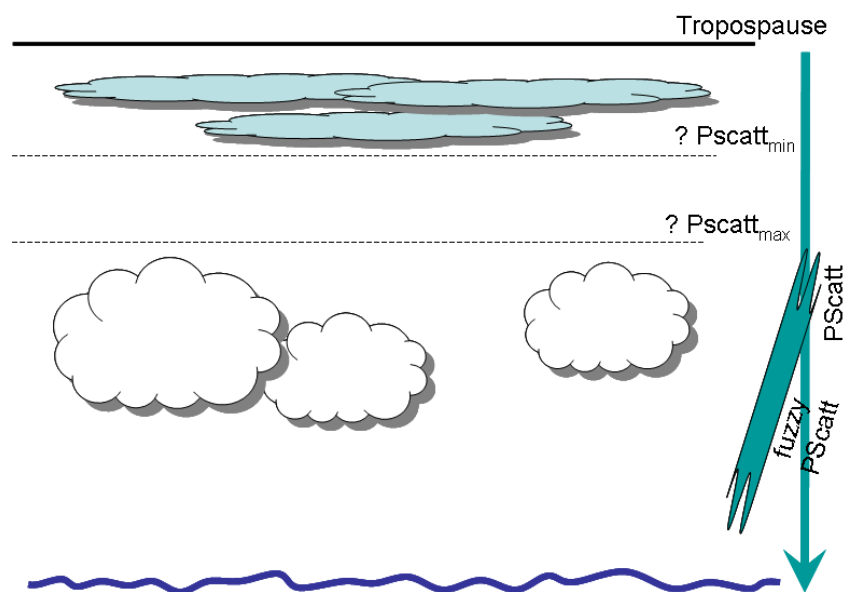
A study has been undertaken to identify this threshold on Pscatt and to study its dependency from time and location. Because Pscatt is particularly useful for the detection of thin cirrus clouds, it was investigated if this threshold could be linked to the height of the troposphere, which varies with latitude and season. In this study 23 MERIS images were investigated (Table 2). In each of the images Pscatt\_min and Pscatt\_max were determined visually by an experienced scientist (Figure 6). Pscatt\_min is the value below which most cirrus clouds are located in an image. Pscatt\_max is the value above which the ambiguous zone starts, where clouds and ocean have the same or even reverse Pscatt values. The main question for this study was, if Pscatt\_min is for all scenes below Pscatt\_max for all scenes. If such a globally applicable value would not exist, it would not be possible to undoubtedly identify cirrus clouds with a global threshold.

Figure 7 presents the result of the study. The 23 images were grouped into classes according to their time/location. The figure shows in blue Pscatt\_min and as a red line Pscatt\_max that was found for all images. Additionally the light blue curve shows the lowest Pscatt found in the images, which indicates the upper height of the clouds found in the images.

While the lowest Pscatt (upper height of the clouds) shows the expected dependency from the latitude (low in the Arctic and high in the tropics), Pscatt\_min does not significantly

depend on time or location. For  $P_{scatt\_max}$  it was very difficult to establish a value per image. The transition from undoubtedly identified clouds to the ambiguous zone is continuous and subjective. However, a global value of 680hPa seems to be good generally applicable value.

It can be concluded from this analysis that the “corridor” between the necessary minimum threshold for  $P_{scatt}$ , and the value where the ambiguous zone starts is rather small, but it exists. A value of 680hPa would fit with almost all images. Only in one of the examined cases, some cirrus clouds would be left out with this threshold.



**Figure 6: Schematic sketch of the  $P_{scatt}$  threshold determination**

Zone	MERIS Product
highlat	MER_RR_2MEPIX20080721_080207_000002002070_00293_33413_0161:
highlat	MER_RR_2MEPIX20080716_104010_000002002070_00223_33343_0159:
highlat	MER_RR_2MEPIX20080720_115510_000002002070_00281_33401_0160:
highlat	MER_RR_2MEPIX20081206_112430_000002002074_00266_35390_0157:
highlat	MER_RR_2MEPIX20081217_035535_000002002074_00419_35543_0158:
highlat	MER_RR_2MEPIX20081203_111639_000002002074_00223_35347_0156:
midlat-summer	MER_RR_2MEPIX20080731_212204_000002002070_00444_33564_0139:
midlat-summer	MER_RR_2MEPIX20080808_120529_000002002071_00052_33673_0135:
midlat-summer	MER_RR_2MEPIX20080710_222026_000002002070_00144_33264_0136:
midlat-summer	MER_RR_2MEPIX20080709_224954_000002002070_00130_33250_0142:
midlat-summer	MER_RR_2MEPIX20080720_120334_000002002070_00281_33401_0134:
midlat-winter	MER_RR_2MEPIX20081122_131227_000002002074_00067_35191_0149:
midlat-winter	MER_RR_2MEPIX20081202_212403_000002002074_00215_35339_0152:
midlat-winter	MER_RR_2MEPIX20081214_132208_000002002074_00382_35506_0151:
midlat-winter	MER_RR_2MEPIX20081231_211340_000002002075_00129_35754_0153:
midlat-winter	MER_RR_2MEPIX20081228_210557_000002002075_00086_35711_0155:
midlat-winter	MER_RR_2MEPIX20081205_112744_000002002074_00252_35376_0150:
tropical	MER_RR_2MEPIX20080616_114246_000002002069_00295_32914_0130:
tropical	MER_RR_2MEPIX20080601_011340_000002002069_00074_32693_0128:
tropical	MER_RR_2MEPIX20080720_221719_000002002070_00287_33407_0133:
tropical	MER_RR_2MEPIX20080630_042223_000002002069_00491_33110_0129:
tropical	MER_RR_2MEPIX20080731_113053_000002002070_00438_33558_0131:
tropical	MER_RR_2MEPIX20080720_171723_000002002070_00284_33404_0132:

Table 2: List of scenes used for the Pscatt threshold determination

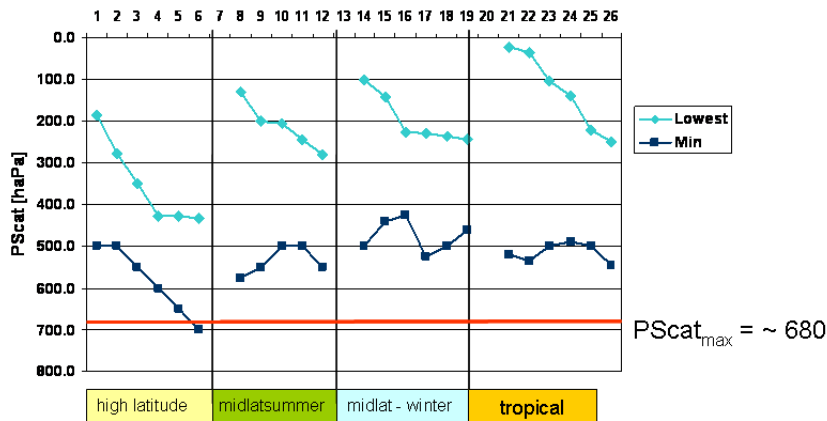


Figure 7: Result of the Pscatt threshold determination study.

Pscatt requires a sufficient number of photons to reach the sensor. Over the ocean these photons should come from the atmosphere, i.e. due to scattering at aerosol molecules or clouds. In cases of clear atmosphere there is a risk that too few photons reach the sensor to permit a valid Pscatt retrieval. This is, for example, the case for clear arctic atmosphere. It is therefore necessary to include a lower threshold for the reflectance in band 10 (or band 12).



### 2.2.3 Sea Ice

Sea ice is often snow covered and can be detected using the MERIS Differential Snow Index (MDSI) as described in section 2.2.6.

### 2.2.4 High glint

Over high glint the bright test are critical because of the bright surface. However, the Pscatt test is rather insensitive against glint. It is therefore possible to deactivate one or all of the bright tests for high glint and rely solely on the Pscatt test.

### 2.2.5 Clouds Over Land

#### 2.2.5.1 Bright Test

One simple blue band test is applied to detect the most brilliant dense clouds. This test has been designed to work with band 2 at 442nm, and a table of the maximum reflectance that could be expected over land surfaces with a standard atmosphere has been calculated. This table provides the threshold for a given sun and viewing geometry.

#### 2.2.5.2 Height of the Scattering Surface (Land)

The basic principle of estimating the apparent height of the scattering surface has been described in section 2.2.2.2. Over land the situation is more difficult:

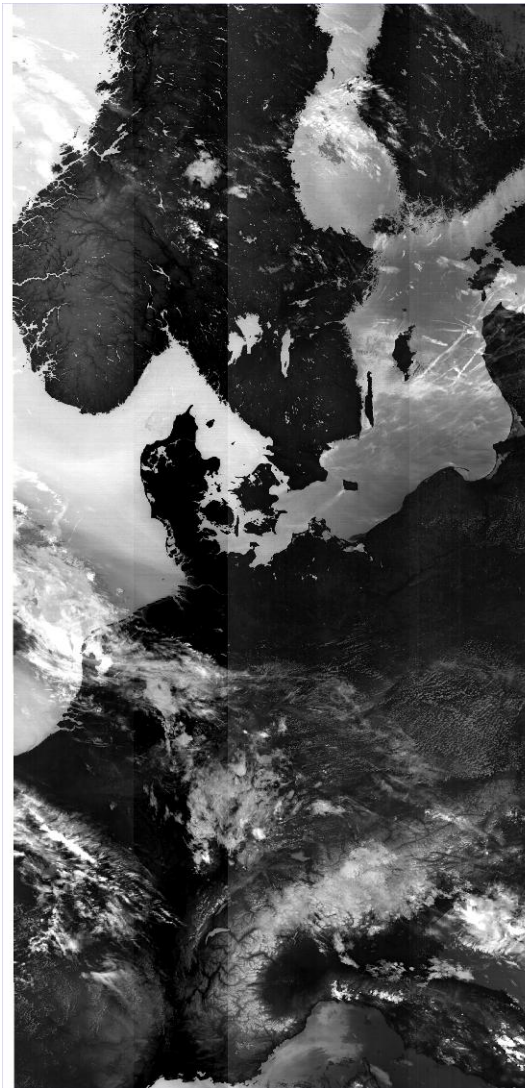
- The underlying surface is not black but can have any albedo. In the algorithm we cannot make any assumption about the ratio of photons from the cloud and from below; this leads to a greater uncertainty
- The underlying surface can be elevated. This has to be taken into account when the retrieved value of the apparent height of the scatterer is compared with a threshold. This has to be terrain dependent, and the quality of the DEM used for comparison has an impact on the quality of the cloud screening.

The first step of the pressure algorithm as presented in section 2.2.2.2, which simply relates the transmission to an apparent height, can be applied also over land. Neither the Rayleigh correction, nor the Fresnel correction can be applied since they make assumptions on the underlying surface which are not given over land.

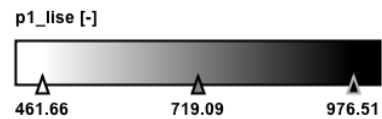
The derived rough estimate of the scattering height (also called P1) is then compared with the height of the DEM. If the difference exceeds a threshold a cloud can be assumed. In

MERIS processing a DEM is available at the tie-point grid. Section 2.3.3 presents a discussion of the use of this coarse grid in comparison with the better resolved and more accurate GETASSE DEM.

An example of the P1 product is shown below in Figure 8:



The image on the left shows the p1 product, which has been tailored to work over land, here is computed over all surfaces. Bright means high altitude scattering target, dark is a low altitude scattering target.



Two observations should be mentioned first:

- the thin clouds/contrails (3) are very well visible as bright = high target
- the bright colour above the Alpes represent the high altitude of these pixels

**Figure 8: Example of the P1 pressure product.**

It has been tried to find a value interval, which could be used to identify clouds over land just by using the computed value. This attempt failed due to the high varying altitude of land pixels.

The relationship between the altitude and the p1 value has led to another exercise: what about the difference between the barometric pressure resulting from the pixel's altitude and the p1 pressure?

With VISAT, the elevation band has been created from the GETASSE30 DEM to have the elevation in better resolution than from the tie points. Using VISAT's band arithmetic, the barometric has been computed from the elevation by using this simplified formula:

$$P_{\text{barometric}} = 1013.25 \left( 1 - \frac{0.0065 * \text{elevation}}{288.15} \right)^{5.255}$$

Using VISAT band arithmetic, the difference between  $p_{\text{barometric}}$  and  $p_1$  has been computed. The result showed that one could identify clouds by using a threshold on the computed difference. For all investigated scenes, the value of 125 hPa turned out to be a threshold.

However, in some cases over dark surface the P1 pressure test indicates pixels wrongly. This is due to the fact that a sufficient number of photons must be transmitted through the atmosphere so that a pressure estimate can be calculated from the differential absorption. If there is a dark surface with no cloud or an optically thin cloud above, very few photons are reflected from the surface and the pressure estimate is quite unsecure. Therefore, a lower limit on the surface reflectance should be set, before the P1 pressure test can be applied. It is proposed to interpolate linearly the reflectance between bands 10 and 12 to the wavelength of band 11, and to set the threshold in the Rayleigh corrected reflectance for this interpolated band.

Empirically it was found that a threshold  $R_{10\_12\_thresh} = 0.15$  works fine.

### 2.2.5.3 Distinction of clouds from bright land surfaces

Figure 7 also illustrates that a second test based on the ratio 443 nm / 750 nm may help discriminating clouds from bright surfaces. For example, if we select, for the geometry of Figure 7, a threshold at 0.7, these bright pixels are identified as land. A limitation to that approach is the spectral variability of sands depending of their origin and humidity level (Table 3). For example, Cosnefroy et al. (1996) report that reflectances for Saharan sands may vary by a factor of 4 between the blue and the red. The same threshold of 0.7 will then correspond to clouds with a larger optical depth in order to smooth the spectral difference. The value of the ratio 443 nm / 750 nm will also be variable due to this spectral variability: for example, for the White Sands Missile Range site and dry sand dunes, the ratio is very close to 1.0 meaning that the absorption in the blue is rather small while it can reach 0.23 for Saharan sand where absorption in the blue is apparently very strong. Establishing a simple threshold value will therefore be quite challenging.

## 2.2.6 Snow and Ice Detection

The Normalised Differential Snow Index (NDSI) is exploiting the decrease of reflectance from VIS-red or NIR to SWIR. NDSI is applied to AATSR, AVHRR or MODIS, where SWIR bands are available. The MERIS Differential Snow Index (MDSI) is using MERIS bands at 865nm and 885nm to simulate the NDSI. The MDSI concept has been developed by R. Preusker (FU Berlin) in the framework of the MERIS AlbedoMap project.

$$MDSI = \frac{\rho_{toa}(865) - \rho_{toa}(885)}{\rho_{toa}(865) + \rho_{toa}(885)}$$

$\rho_{toa}$  is the top of atmosphere reflectance.

If a pixel, that has been proven to be bright beforehand, has  $MDVI > 0.01$ , then it can be considered as snow or ice.

A comparison of the MDSI flagged pixel with the AATSR NDSI has been made for orbit 21934, 11.05.2006. For an area over the Alpes, which is in the centre of the orbit and where MERIS and AATSR measurements are available, the AATSR-NDSI has been calculated. The whole rectangular area, and those pixels flagged by the MDSI are shown in Figure 9. The frequency distribution of the AATSR-NDSI is shown in Figure 10 for the whole subset, and for the MDSI flagged pixels. The ratio of the two numbers is also included in the figure. One can see that almost all pixels with a high AATSR-NDSI are covered by the MDSI flag, and the low-NDSI pixels are excluded. Assuming that the AATSR-NDSI is a good indicator for snow, this results is an indication that the MDSI test is catching the right pixels.

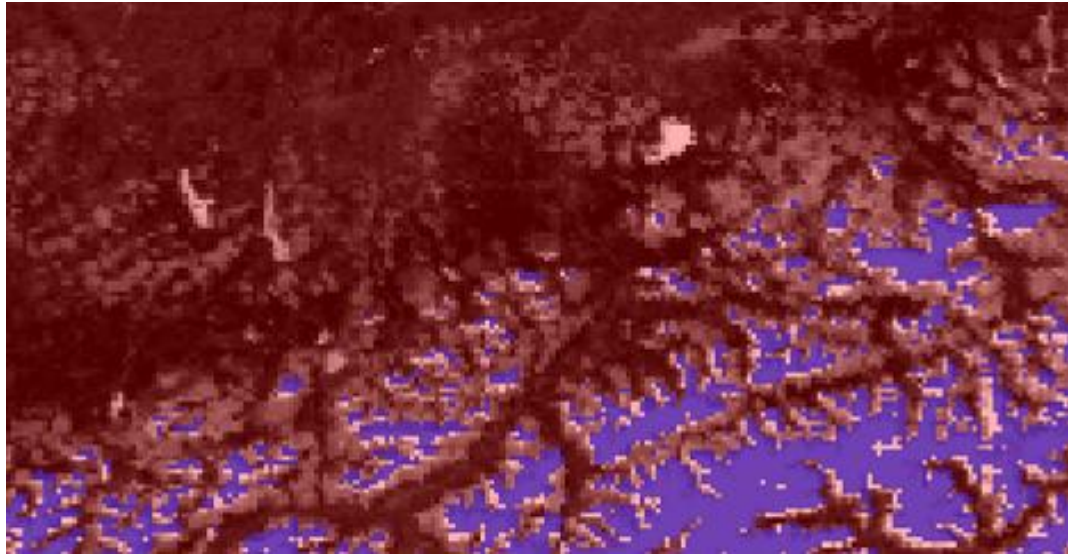


**Figure 9: Subset of Orbit 21934, 11.05.2006, including part of the Alpes and of the flat pre-Alpes. The AATSR NDSI has been calculated for the whole area, and those pixels which are flagged by the MDSI (blue).**

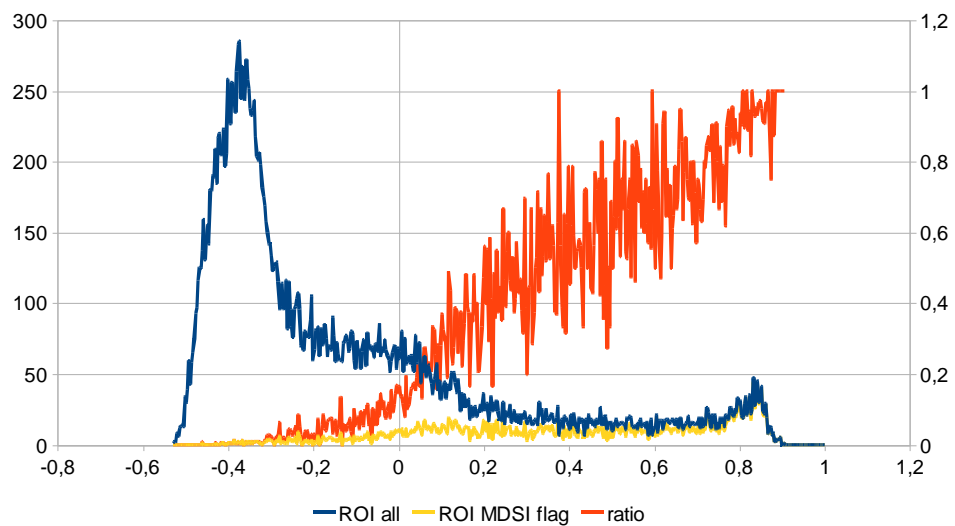


**Figure 10: AATSR-NDSI for all pixel of the area shown in Figure 9 (blue), and for those pixels which are flagged as snow by the MDSI test (yellow). The ratio  $NDSI\_MDSI / NDSI\_ALL$  is shown as red line.**

## 2.3 Practical Considerations

### 2.3.1 Land – Water Classification

The purpose of this classification is to identify using geo-physical data, land from water pixels in cases where the Level1b a priori classification leads to ambiguities which may occur from:

- geo-location error;
- land /ocean atlas error: uncharted land or water, etc.;
- transient emerged land: tidal flats, etc.

This cases are identified using a Surface Confidence Map, an atlas identifying zones of low confidence in the a priori land/water classification map used in the level1b. When the Surface Confidence Map indicates high confidence classification, the Land Identification radiometric tests are by-passed and the a priori classification is kept.

#### 2.3.1.1 Inland water

First, a test on the reflectance corrected for gaseous absorption at 665 nm is performed to identify the darkest pixels. The TOA reflectance at 665 nm is compared to a threshold interpolated from a LUT.

For the pixels having a reflectance smaller than this threshold, a second test is made to compare the TOA reflectance at 665 nm with the TOA reflectance at 865 nm; if the TOA reflectance at 665 nm is greater than the reflectance at 865 nm, the pixel is classified as water.

#### 2.3.1.2 Land in water

The purpose of this test is to identify pixels of emerged land, flagged as "water" in the L1B product. It is the opposite of the Inland water test.

### 2.3.2 Cloud Screening

The cloud screening tests different between land and ocean. The L1b land mask is used to switch the algorithm.

### 2.3.2.1 Cloud over the ocean

As clouds are often bright, a first stage screening is done for the determination of bright pixels using tests and auxiliary data values. Two tests are conducted: one using tabulated values for maximum expected marine reflectance for the given geometry over a medium turbid ocean and atmosphere. The second test is comparing the Rayleigh reflectance in the blue with a global threshold.

The Apparent Pressure ( $P_{scatt}$ ) is then computed to allow detection of high altitude thin clouds not captured by the bright tests. The calculation of  $P_{scatt}$  requires strictly an underlying ocean surface and does not work properly over land. Unfortunately the L1b land-water mask is sometime erroneous. Therefore a buffer of a few pixels is placed around the coastline where the  $P_{scatt}$  is not applied.

After identification of cloud candidates by the two bright tests and the pressure test, a test on potential snow/ice is applied to those candidates. In cases of high MDSI values the pixels are identified as snow/ice and not as clouds. The snow/ice pixels over the ocean are included in the ICE\_HAZE flag of the final MERIS L2 product.

Under glint conditions only the first bright test (using tabulated values of precomputed thresholds) and the test on apparent pressure are used.

### 2.3.2.2 Clouds over Land

The cloud screening over land relies on the bright test and the pressure test. After identification of potential clouds using these two tests, the MDSI is applied to these bright targets to sort out snow and ice. The remaining pixels are labelled clouds.

The slopes tests are currently not used.

### 2.3.3 Comparison of pressure computations over land using tie-point DEM and GETASSE DEM

The barometric pressure used for the thresholding should be computed from a DEM which is as accurate as possible. For MERIS, this would be the GETASSE 30 DEM, which is available from ESA and which can be used with BEAM. On the other hand, currently GETASSE is not available during L2 processing, but the MERIS L1 product contains also DEM values at tie-point resolution. The following exercise shall assess the impact on the pixel classification when the tie-point DEM is used instead of the GETASSE 30. The first scene used for the comparison is MER\_RR\_\_2MEPIX20080722\_174153\_000003972070\_00313\_33433\_0536:

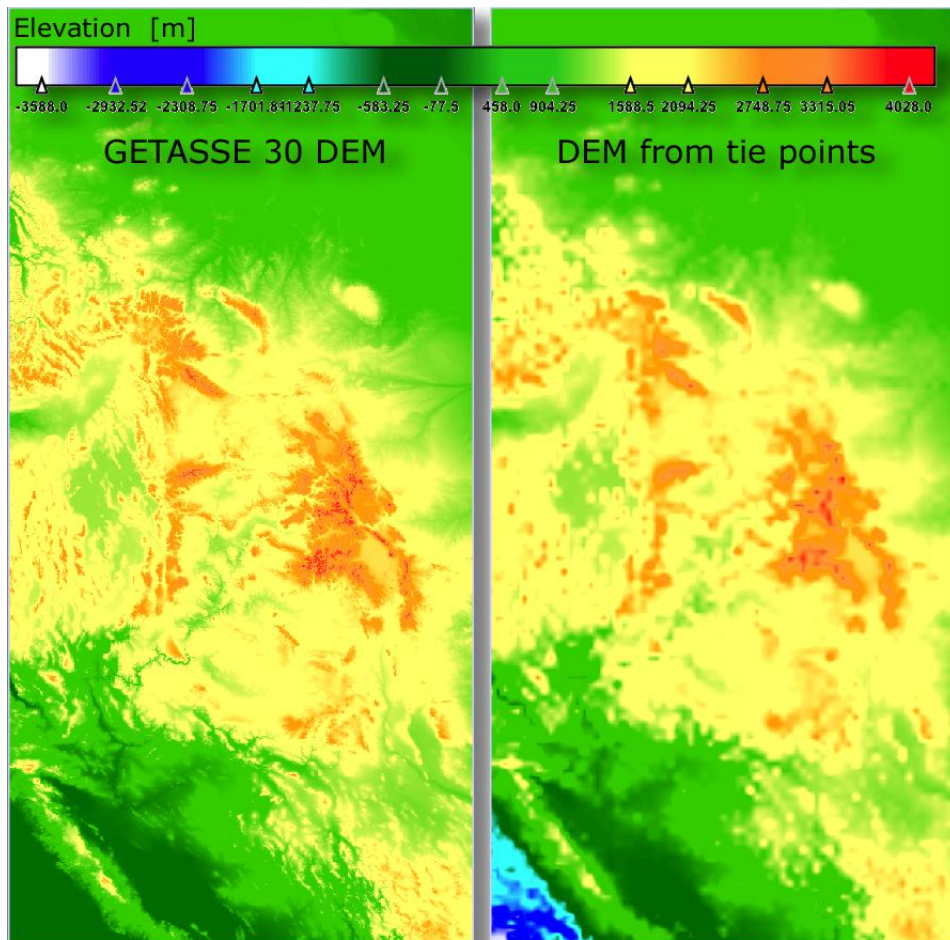


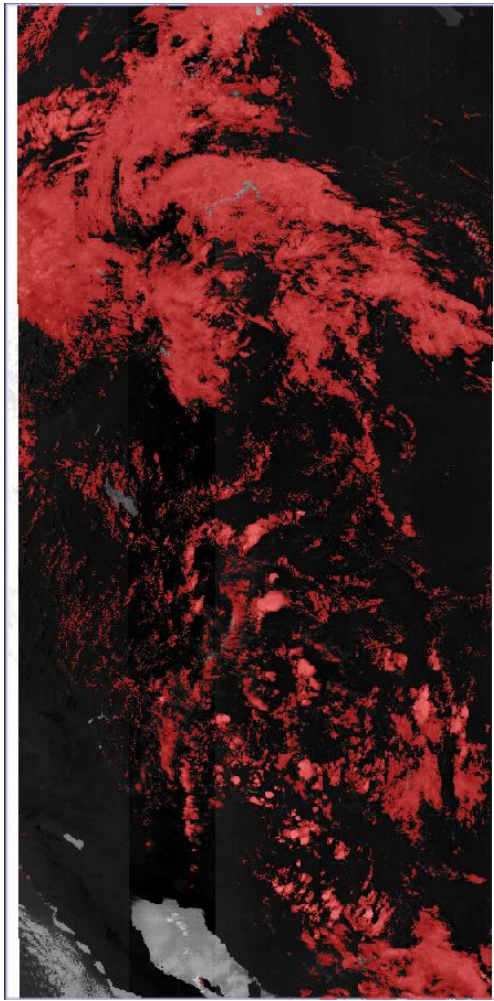
**Figure 11: Visual comparison of GETASSE 30 and tie-point DEM**

As it can be seen from Figure 11, both DEMs are very much in the same order of magnitude over land. Note: for water surfaces, the tie-point DEM in the MERIS L1 products contains bathymetry information, which might have large negative values, whereas the GETASSE 30 DEM shows values around -40m.

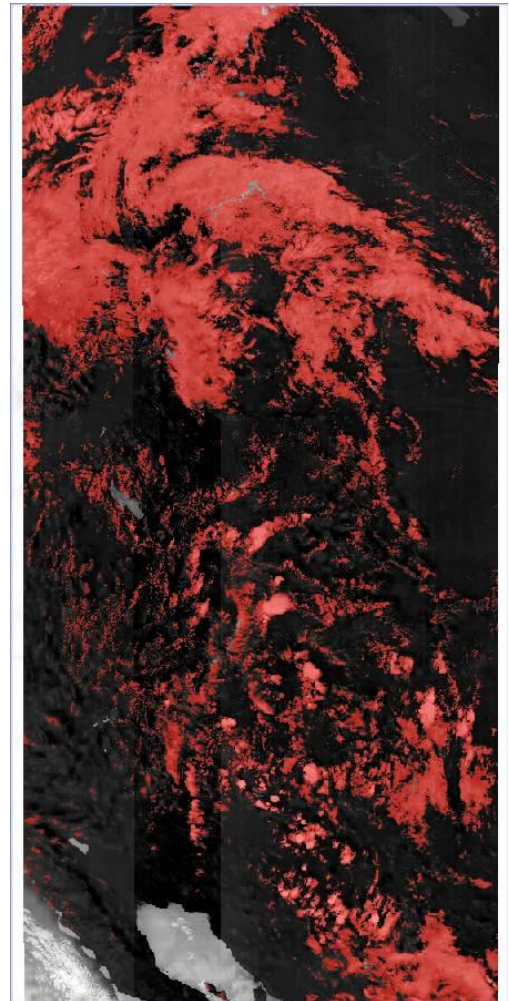
For comparison, the thresholding technique has been applied to the bands:

- p\_barometric\_minus\_p1, with the barometric pressure from the GETASSE 30 DEM,
- p\_barometric\_from\_tp\_minus\_p1 with the barometric pressure from the tie points





p\_barometric\_minus\_p1 >= 125

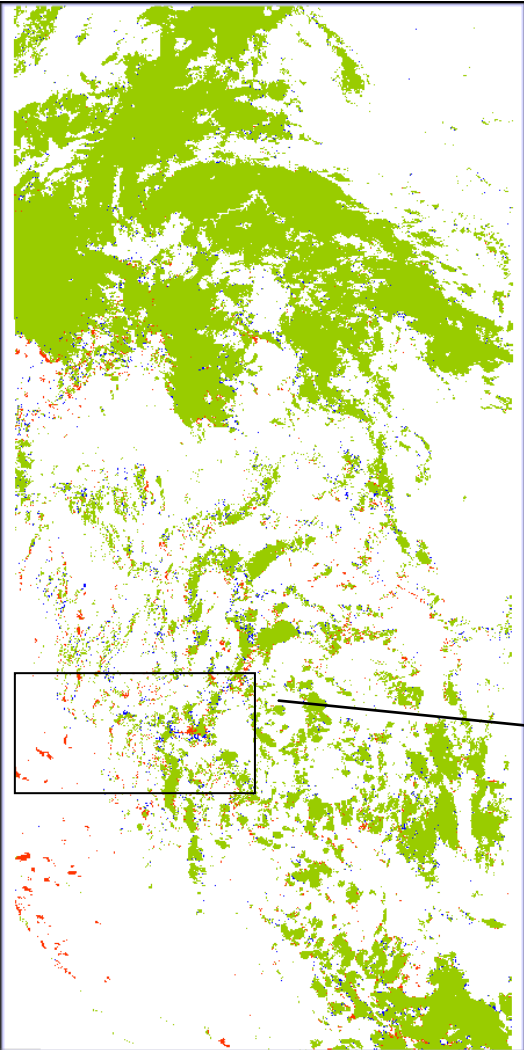
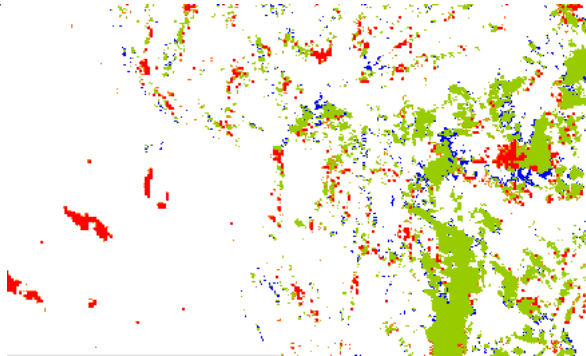


p\_barometric\_from\_tp\_minus\_p1 >= 125

As it can be seen for example in the lower left part of right image, using the tie point DEM leads to some more flagged pixels:

Number of pixels total: 2530097

Band, criterion	Number of flagged pixels	%
p_barometric_minus_p1 >= 125	689198	27.24
p_barometric_from_tp_minus_p1 >= 125	694367	27.44

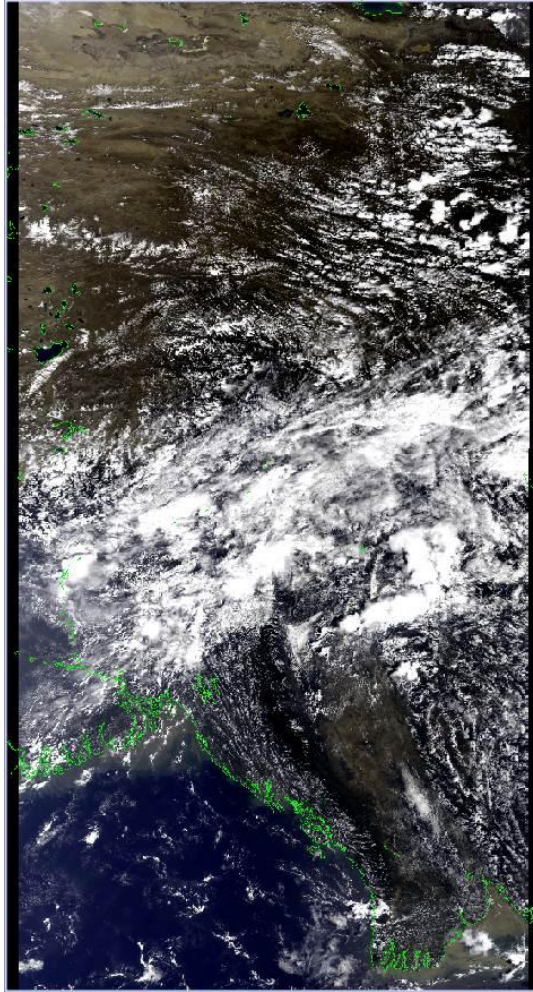
	<p>Comparing the different classification possibilities of the two variants, the image on the left shows the following classes:</p>
	<p>(1) green: both flagged</p> <p>(2) white: both not flagged</p> <p>(3) blue: flagged using GETASSE, not flagged using tie points DEM</p> <p>(4) orange: not flagged using GETASSE, but flagged using tie points DEM</p>
	<p>The image below shows a partial magnification from the overview image on the left:</p> 

In counts:

Number of pixels total: 2530097

<b>class</b>	<b>GETASSE</b>	<b>tie points</b>	<b>number</b>	<b>%</b>
1	true	true	672745	26.59
2	false	false	1819277	71.91
3	true	false	16453	0.65
4	false	true	21622	0.85

In the following product located over Myanmar, the relation is quite similar. However, the number of pixels flagged / not flagged by either variant is nearly identical. There are about 2% of pixels that differ in each direction (see statistics below).



In counts:

Number of pixels total: 2323833

<b>class</b>	<b>GETASSE</b>	<b>tie points</b>	<b>number</b>	<b>%</b>
1	true	true	405141	17.43
2	false	false	1825948	78.57
3	true	false	43652	1.88
4	false	true	49092	2.11

In conclusion, the tie-point DEM can be used for RR products. The classification would be improved by a few percent if the GETASSE DEM would be used.

In Full Resolution the difference between the two DEMs and its impact on the pressure test result has been studied at the example of two MERIS FR product over the Alpes, from 16.11.2005 and 19.11.2005. Figure 12 shows the barometric pressure image of a an

area in the Alpes in full resolution from GETASSE (left) and the Tie Points (right). The difference between the two products is clearly visible. Values are often in the order of  $\pm 100$ hPa and can reach  $\pm 300$ hPa in the valleys or on top of the mountains (Figure 13).

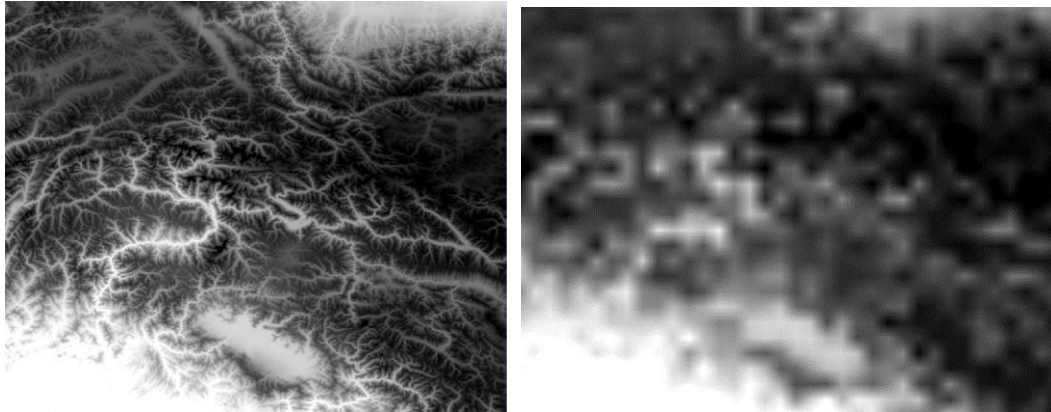


**Figure 12: hPa for the elevation of each pixel: left: DEM GETASSE; right: DEM TiePoints**

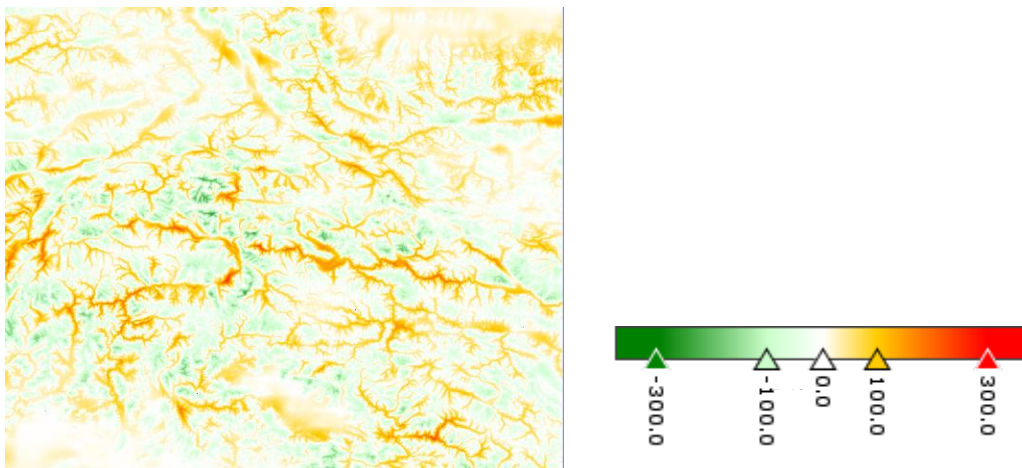


**Figure 13: difference of both dem-pressure images**

If we assume that the GETASSE DEM is correct and the Tie-Point DEM is wrong due its coarser resolution, we can run the snow-cloud screening on the GETASSE DEM (“truth”) and compare it with the snow-cloud screening on the Tie-Point DEM. Pixels which are classified differently are then considered as wrong in this comparison. The result of this test is shown in Figure 14 (16.12.05, clouds over snow in the North, clear sky snow in the centre, clear sky no snow in the south) and Figure 15 (19.11.05, only snow and clear sky, only a few clouds over no snow in the snow) below. Pixels which are classified as clouds in the Tie-Point version but not in the GETASSE processing are marked in red. It can be

seen that a limited number of pixels are affected at the border of the Alpes. It depends on the user requirements if this amount (and the location) of these misclassified pixels matters or not.

In conclusion one can say that for FR processing using the GETASSE brings a clear advantage over the Tie-Point DEM, and if possible, it should be used for operational processing. However, using the Tie-Point DEM is doing a reasonable job in many cases.

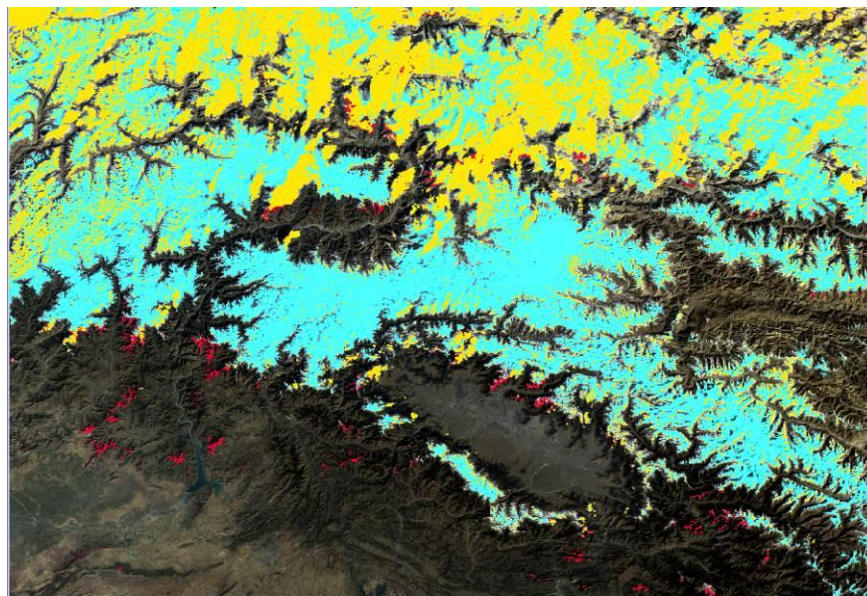
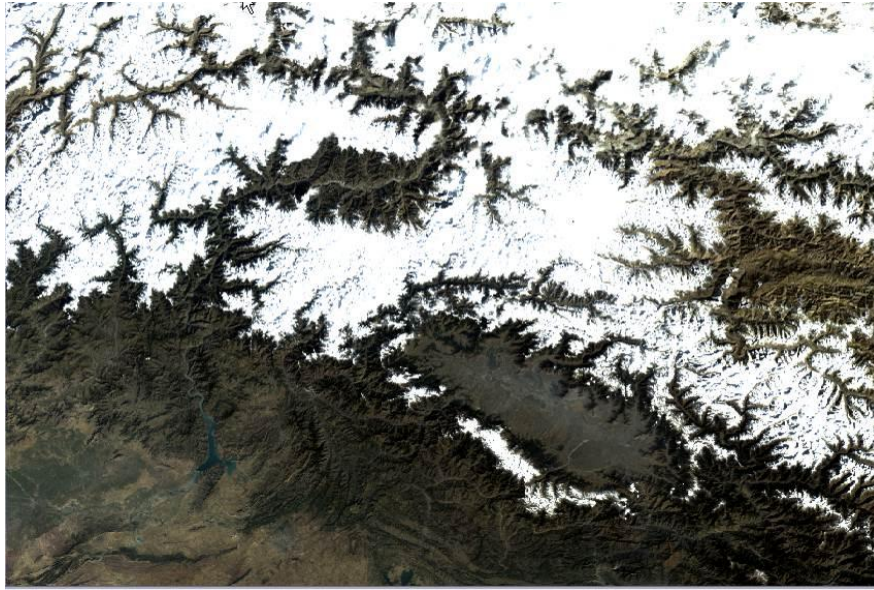


**Figure 14: Influence of GETASSE and Tiepoint DEM on the cloud identification: blue: snow; yellow: cloud\_flag derived from getasse30, red: additional pixels classified as cloud using the tie\_point DEM; product: 16.11.2005**

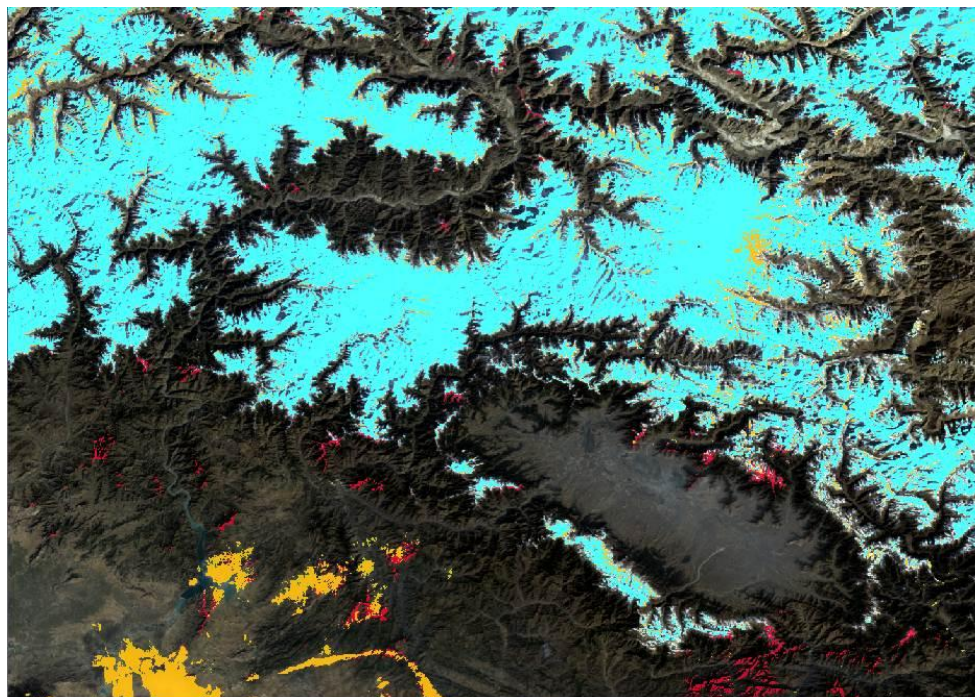
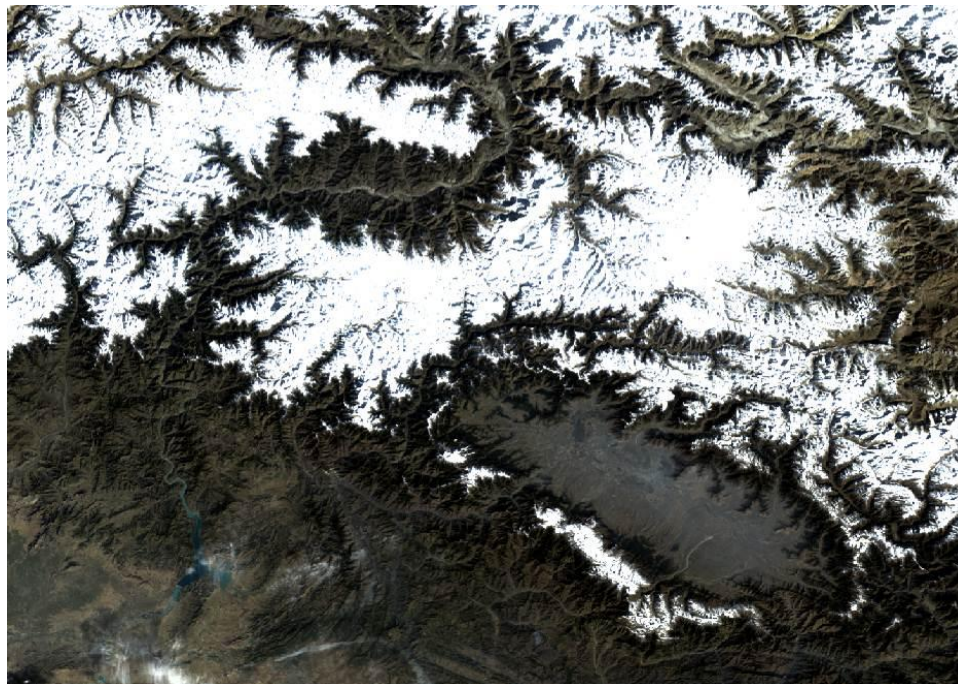


**Figure 15: Influence of GETASSE and Tiepoint DEM on the cloud identification: blue: snow; yellow: cloud\_flag derived from getasse30, red: additional pixels classified as cloud using the tie\_point DEM; product: 19.11.2005**

### 3. ERROR BUDGET ESTIMATES

Estimation of the error of a classification requires a true reference. “True” can be easily established for a totally cloudy or a totally cloud free pixel, however, the critical pixels are semi-transparent pixels, which cannot be processed by the atmospheric correction. Hence, the error of the pixel identification cannot be established on its own but only in connection with the atmospheric correction.

A compromise in this respect is to establish a true reference of pixels labeled “100% cloud”, “100% clear sky” and “partly cloudy”. Such a reference dataset is currently being collected by manually classifying a large number of MERIS image pixels. The classification is done according to the classification scheme presented below. The collection is a long time process, and in an update of this ATBD we will be able to use this database and quantify the error of the pixel classification on the basis of these three categories.

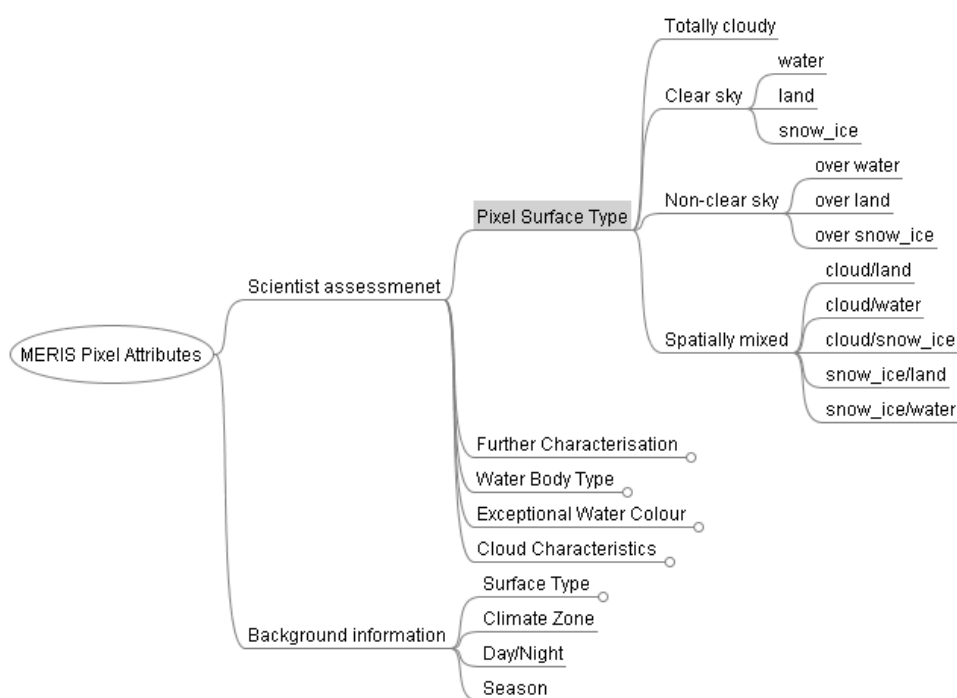


**Figure 3-1: Classification structure**

## 4. ASSUMPTIONS AND LIMITATIONS

The following assumptions apply:

- The products to be processed are MERIS Reduced Resolution or Full Resolution products.
- The algorithm has to run fully automatic.
- The algorithm parameters shall not depend on values derived from scene statistics (e.g. histograms calculated from the scene to be processed).

The following limitations of the Pixel Identification are known:

- The glint calculation is making use of the wind speed at tie-points. This wind speed comes from the 3h numerical weather forecast. This is typically much different from the actual windspeed at surface at the moment of the data take. Hence, the estimation of the glint affected area is not precise especially at the edge of the sun glint area.
- The algorithm is supposed to be applied global and to whole mission. As a consequence a local tuning of the algorithm is not permitted. Individual scenes will then not be as good classified as if a local tuning to that scenes would have been applied.



## 5. REFERENCES

Ackerman, S., K. Strabala, P. Menzel, R. Frey, C. Moeller, L. Gumley, B. Baum, S. WetzelSeemann, and H. Zhang: Discriminating clear sky from cloud with MODIS algorithm theoretical basis document (MOD35), at [http://modis.gsfc.nasa.gov/data/atbd/atbd\\_mod06.pdf](http://modis.gsfc.nasa.gov/data/atbd/atbd_mod06.pdf), 2006.

Albert, M.R., Shuman, C., Courville, Z., Bauer, R., Fahnestock, M., and Scambos, T.: Extreme Firn Metamorphism: Impact of Decades of Vapor Transport on Near-Surface Firn at a Low-Accumulation Glazed Site on the East Antarctic Plateau. *Annals Glaciol.*, 39, 73-78, 2004.

Alley, R.B., and Koci B.R.: Ice-core analysis at site A, Greenland : preliminary results. *Annals Glaciol.* 10, 1-4, 1988.

Alley, R.B., Saltzman, E.S., Cuffey, K.M. and Fitzpatrick, J.J., Summertime formation of depth hoar in central Greenland. *Geophys. Res. Lett.*, 17, 2393-2396, 1990.

Aoki, T., Aoki, T., Fukabori, M., Hachikubo, A., Tachibana, Y. and Nishio, F., Effects of snow physical parameters on spectral albedo and bidirectional reflectance of snow surface. *J. Geophys. Res.*, 105D, 10219-10236, 2000.

Aoki, T., M. Hori, H. Motoyoshi, et al., ADEOS-II/GLI snow/ice products — Part II: Validation results using GLI and MODIS data. *Remote Sensing Environ.*, 111, 274-290, 2007.

Baret, F, et al, LAI, fAPAR and fCover CYCLOPES global products derived from VEGETATION Part 1: Principles of the algorithm. *Remote Sensing of Environment*, Volume 110, Issue 3, 15 October 2007, Pages 275-286, 2007.

Birks et al, Improvements to the AATSR IPF relating to Land Surface Temperature Retrieval and Cloud Clearing over Land, RUTHERFORD APPLETON LABORATORY, 2007.

Bohren, C. F., and Barkstrom, B. R., Theory of the optical properties of snow, *J. Geophys. Res.*, 79, 4527-4535, 1974.

Bohren, C. F., and Beschta, R. L., Snowpack albedo and snow density, *Cold Regions Sci. Technol.*, 1, 47-50, 1979.

Bourdelles, B., and Fily, M., Snow grain-size determination from Landsat imagery over Terre Adelie, Antarctica, *Annals Glaciol.*, 17, 86-92, 1993.

Brenguier, J.-L., H. Pawlowska, L. Schüller, R. Preusker, J. Fischer and Y. Fouquart, Radiative properties of boundary layer clouds: droplet effective radius versus droplet concentration. *J. Atmos. Sci.*, 57, 803-821, 2000.

Brockmann et al, Cloud Screening Algorithms, MERIS - AATSR Workshop, 2008. ESRIN, Frascati, Italy; Workshop Proceedings, 2008.

Brunauer, S., Emmet, P.H. and Teller, E.: Adsorption of gases in multimolecular layers. *J. Am. Chem. Soc.* 60, 309-319, 1938.

Cervino et al, Cloud fraction within GOME footprint using a refined cloud clearing algorithm, *Adv. SpaceRes.* Vol. 25, No. 5, pp. 993-996, 2000.

Chandrasekhar, S., Radiative transfer, NY: Dover, 1960.

Colapicchioni et al, Information Mining in Remote Sensing Image - The KIM, KES and KIMV projects, ESA ESRIN Publication, 2004.

Colbeck, S.C., An overview of seasonal snow metamorphism, *Rev. Geophys. Space Phys.* 20, 45-61, 1982.

Colbeck, S.C., Theory of metamorphism of dry snow, *J. Geophys. Res.* 88, 5475-5482, 1983.

Colbeck, S.C., The layered character of snow covers, *Rev. Geophys.* 29, 81-96, 1991.

D'Elia et al, Image Information Mining for Earth Observation at ESA, ESA ESRIN Publication, 2004.

Domine, F., Taillandier, A.-S. and Simpson W.R., A parameterization of the specific surface area of snow in models of snowpack evolution, based on 345 measurements. *J. Geophys. Res.*, 112, F02031, doi:10.1029/2006JF000512, 2007.

Domine, F., Salvatori, R., L. Legagneux, L., Salzano, R., Fily M. and R. Casacchia R., Correlation between the specific surface area and the short wave infrared (SWIR) reflectance of snow: preliminary investigation. *Cold Regions Sci. Technol.*, 6, 60-68, doi:10.1016/j.coldregions.2006.06.002, 2006.

Domine F., M. Albert, T. Huthwelker, H.-W. Jacobi, A. A. Kokhanovsky, M. Lehning, G. Picard, W. R. Simpson, Snow physics as relevant to snow photochemistry, *Atmos. Chem. Physics Discussions*, 7, 1-96, 2008.

Domingue, D., et al., The scattering properties of natural terrestrial snows versus icy satellite surfaces, *Icarus*, 128, 28-48, 1997.

Dozier, J., and S. G. Warren, Effect of viewing angle on the thermal infrared brightness temperature of snow, *Water Resour. Res.*, 18, 1424-1434, 1982.

Dozier, J., and Painter, T. H., Multispectral and hyperspectral remote sensing of alpine snow properties. *Annual Review of Earth and Planetary Sciences* 32, 465-494, 2004.

Eumetsat, Final Report for the Study on Visual Scenes Analysis of AVHRR Data, Issue 2, 16. January 2006.

Eumetsat, Summary Report of the SAF Hydrology Framework Working Group  
[http://www.eumetsat.int/groups/pps/documents/assets/pdf\\_saf\\_hsfwg\\_summaryreport.pdf](http://www.eumetsat.int/groups/pps/documents/assets/pdf_saf_hsfwg_summaryreport.pdf), 2004

Eumetsat, Land Surface Analysis Satellite Application Facility, Snow Cover product,  
<http://landsaf.meteo.pt/algorithms.jsp;jsessionid=4745E8FF3EBC82A5D6C69D5FE6838E99?seltab=4>, 2008

Euroclim Website, Euroclim Website <http://www.euroclim.net/>, 2008

European Space Agency, Statement of work Globice, EOP-DUEP-EOPS-SW-04-0006  
[http://dup.esrin.esa.it/files/document/192-171-5-19\\_200483011918.pdf](http://dup.esrin.esa.it/files/document/192-171-5-19_200483011918.pdf), 2004

European Space Agency, Statement of work GlobGlacier, EOEP-DUEP-EOPG-SW-06-0005,  
[http://dup.esrin.esa.it/files/document/131-176-149-30\\_200828162037.pdf](http://dup.esrin.esa.it/files/document/131-176-149-30_200828162037.pdf), 2006

European Space Agency, STATEMENT OF WORK GLOBSNOW, EOEP-DUEP-EOPS-SW-08-0006,  
[http://dup.esrin.esa.int/STSE/files/document/131-176-149-30\\_200865103541.pdf](http://dup.esrin.esa.int/STSE/files/document/131-176-149-30_200865103541.pdf), 2008

Fily, M., Bourdelles, B., Dedieu J.P., and Sergent, C., Comparison of in situ and Landsat Thematic Mapper derived snow grain characteristics in the Alps, *Remote Sensing Environ.*, 59, 452–460, 1997.

Fischer, J. et al, MERIS ESL Cloud Cloud Top Pressure ATBD.  
[http://envisat.esa.int/instruments/meris/pdf/atbd\\_2\\_03.pdf](http://envisat.esa.int/instruments/meris/pdf/atbd_2_03.pdf), 2000a.

Fischer, J. et al, MERIS ESL Cloud Albedo and Cloud Optical Thickness ATBD.  
[http://envisat.esa.int/instruments/meris/pdf/atbd\\_2\\_01.pdf](http://envisat.esa.int/instruments/meris/pdf/atbd_2_01.pdf), 2000b.

Flanner, M. G.; Zender, C. S.; Randerson, J. T.; Rasch, Philip J., Present-day climate forcing and response from black carbon in snow. *J. Geophys. Res.*, 112, D11202, .doi:10.1029/2006JD008003, 2007.

Flanner, M.G. and Zender, C.S., Linking snowpack microphysics and albedo evolution. *J. Geophys. Res.* 111, D12208. doi:10.1029/2005JD006834, 2006.

Garant L., and Weinman J. A., A structural stochastic model for the analysis and synthesis of cloud images. *J. Clim. Appl. Meteorol.* 25, 1052-1068, 1986.

Garret, T. J., P. V. Hobbs, H. Gerber, Shortwave, single scattering properties of arctic ice clouds, *J. Geophys. Res.*, 106, D14, 15,555-15,172, 2001.

GCOS home page, <http://www.wmo.int/pages/prog/gcos/index.php?name=about>

Globsnow user consultation meeting, presentations, <http://dup.esrin.esa.int/news/news152.asp>, 2008

Gomez-Chova et al, Cloud-Screening Algorithm for ENVISATMERIS Multispectral Images, *IEEE TRANSACTIONS ON GEOSCIENCE AND REMOTE SENSING*, VOL. 45, NO. 12, December 2007

Goodman et al, Cloud Detection and Analysis A Review of Recent Progress, *Atmospheric Research*, 21 (1988) 203-228, 1988.

Grenfell, T. C., Perovich, D. K., and Ogren J. A., Spectral albedos of an alpine snowpack, *Cold Regions Sci. Technol.*, 4, 121-127, 1981.

Grenfell, T. C., Warren, S. G., and Mullen, P. C., Reflection of solar radiation by the Antarctic snow surface at ultraviolet, visible, and near-infrared wavelengths, *J. Geophys. Res.*, 99, 18669-18, 684, 1994.

Hall, D.K., Riggs G.A. and Salomonson, V.V. , Development of methods for mapping global snow cover using Moderate Resolution Imaging Spectroradiometer (MODIS) data *Remote Sensing of Environment*, vol. 54, pp. 127-140, 1995.

Hall D.K., Riggs, G. A. and Salomonson, V., Algorithm Theoretical Basis Document (ATBD) for the MODIS Snow and Sea Ice-Mapping Algorithms, available at [http://modis.gsfc.nasa.gov/data/atbd/atbd\\_mod10.pdf](http://modis.gsfc.nasa.gov/data/atbd/atbd_mod10.pdf), 2001.

Hapke, B., [Theory of Reflectance and Emittance Spectroscopy \(Topics in Remote Sensing\)](#), Cambridge: Cambridge University Press, 1993.

Hori, M., et al: In situ measured spectral directional emissivity of snow and ice in the 8-14  $\mu m$  atmospheric window, *Remote Sens. Of Env.*, 100, 486-502., 2006

Hori, M., T. Aoki, K. Stamnes, W. Li, [ADEOS-II/GLI snow/ice products — Part III: Retrieved results](#), *Remote Sensing of Environment*, 111, 291-336, 2007.

Hudson S. R., S. G. Warren, R. E. Brandt, T. C. Grenfell, D. Six, Spectral bidirectional reflectance of Antarctic snow: Measurements and parameterization, *J. Geophys. Res.*, 111, D18106, doi:10.1029/2006JD007290, 2006.

IGOS, Concept of an IGOS-Cryosphere Theme(IGOS-Cryo),  
[http://www.igospartners.org/docs/theme\\_reports/IGOS\\_Cryo\\_theme\\_item7.2.pdf](http://www.igospartners.org/docs/theme_reports/IGOS_Cryo_theme_item7.2.pdf) , 2005

IGOS home page, <http://www.igospartners.org/over.htm>, 2008

Kerbrat, M., Pinzer, B., Huthwelker, T., Gäggeler, H. W., Ammann, M., and Schneebeli M.: Measuring the specific surface area of snow with X-ray tomography and gas adsorption: comparison and implications for surface smoothness. *Atmos. Chem. Phys. Disc.*, 7, 10287-10322, 2007.

King J.C., M.J. Varley, T.A. Lachlan-Cope, Using satellite thermal infrared imagery to study boundary layer structure in an Antarctic katabatic wind region. *Int. J. Remote Sens.* :3335–48, 1998.

King M.D. and Simpson, W.R., Extinction of UV radiation in Arctic snow at Alert, Canada (82° N), *J. Geophys. Res.*, 106 (D12), 12499-12508, 2001.

Klein, A.G. Hall D.K. and Riggs G.A., Improving the MODIS global snow-mapping algorithm." Proceedings of the International Geoscience and Remote Sensing Symposium (IGARSS 1997), 4-8 August 1997, Singapore, pp. 619-621, 1997

Koendrink, J. J. and W.A. Richards, 1992: Why snow is so bright, *JOSA*, A5, 643-648.

Kokhanovsky, A. A., and E. P. Zege, Scattering optics of snow, *Appl. Optics*, 43, 1589-1602, 2004.

Kokhanovsky, A. A., T. Aoki, A. Hachikubo, M. Hori, E. P. Zege, Reflective properties of natural snow: approximate asymptotic theory versus in situ measurements, *IEEE Trans. Geosci. Rem. Sens.*, 43, 1529-1535, 2004.

Kokhanovsky, A. A., and T. Nauss, Satellite based retrieval of ice cloud properties using semianalytical algorithm, *J. Geophys. Res.*, D110, D19206, doi: 10.1029/2004JD005744, 2005.

Kokhanovsky, A. A., On remote sensing of optically thick ice clouds, *Optical Engineering*, 45(4), 046201, 2006a.

Kokhanovsky, A. A., *Cloud Optics*, Dordrecht: Springer, 2006b.

Kokhanovsky, A. A., Scaling constant and its determination from simultaneous measurements of light reflection and methane adsorption by snow samples, *Opt. Letters*, 31, 3282-3284, 2006c.

Kokhanovsky et al, The determination of the cloud fraction in the fraction in the sciamachy pixels using MERIS, MERIS - AATSR Workshop, 2008. ESRIN, Frascati, Italy; Workshop, 2008.

Kottek, M., J. Grieser, C. Beck, B. Rudolf, and F. Rubel, World Map of the Köppen-Geiger climate classification updated. *Meteorol. Z.*, 15, 259-263. DOI: 10.1127/0941-2948/2006/0130, 2006.

Lavanant et al, A global Cloud detection scheme for high spectral resolution instrument, ITSC14 Conference presentation, 2005.

Legagneux, L., Cabanes, A., and Domine, F., Measurement of the specific surface area of 176 snow samples using methane adsorption at 77 K, *J. Geophys. Res.* 107 (D17), 4335, doi: 10.1029/2001JD001016, 2002.

Legagneux, L. Lauzier, T., Dominé, F., Kuhs, W.F., Heinrichs, T., and Techmer, K., Rate of decay of the specific surface area of snow during isothermal experiments and morphological changes studied by scanning electron microscopy. *Can. J. Phys.* 81, 459-468, 2003.

Lenoble, J., *Radiative Transfer in Scattering and Absorbing Atmospheres: Standard Computational Procedures*, Deepak, Hampton, 1985.

Li, W., Stamnes, K., Chen, B., and Xiong, X., Snow grain size retrieved from near-infrared radiances at multiple wavelengths, *Geophys. Res. Lett.*, 28, 1699-1702, doi: 10.1029/2000GL011641, 2001.

Libbrecht, K. G., The physics of snow crystals. *Rep. Prog. Phys.*, 68, 855-895, 2005.

Liou, K.N., *Radiation and Cloud Processes in the Atmosphere*. Oxford University Press, Oxford, 487pp., 1992.

Luo et al, Developing clear-sky cloud and cloud shadow mask for producing clear-sky composites, *Remote Sensing of Environment* 2008; in press, 2008.

Macke, A., Mueller, J. and Raschke, E., Single scattering properties of atmospheric ice crystals. *J. Atmos. Sci.* 53, pp. 2813–2825, 1996.

Matzl, M., and Schneebeli, M.: Measuring specific surface area of snow by near-infrared photography, *J. Glaciol.*, 52, 558-564, 2006.

McNally et al, A cloud detection algorithm for high-spectral-resolution infrared sounders, *Q. J. R. Meteorol. Soc.* (2003), 129, pp. 3411–3423, 2003.

Merchant et al, Probabilistic physically based cloud screening of satellite infrared imagery for operational sea surface temperature retrieval Merchant 2006 SEA SURFACE TEMPERATURE FOR CLIMATE FROM THE ATSRs, Q. J. R. Meteorol. Soc. (2005), 131, pp. 2735–2755, 2005.

Merchant et al, SEA SURFACE TEMPERATURE FOR CLIMATE FROM THE ATSRs, ESA publication, 2006.

Metsämäki, S.J., Anttila, S.T., Markus, H.J. and Vepsäläinen, J., A feasible method for fractional snow cover mapping in boreal zone based on a reflectance model. Remote Sensing of Environment, 95, 2005, pp. 77-95, 2005.

Middleton, W. E. K. and A. G. Mungall, The luminous directional reflectance of snow, JOSA, 42, 572-579, 1952.

Mishchenko, M. I., Dlugach, J. M., Yanovitskij, E. G., Zakharova N. T., Bidirectional reflectance of flat, optically thick particulate layers : an efficient radiative transfer solution and applications to snow and soil surfaces, J. Quant. Spectrosc. Radiat. Transfer, 63, 409-432, 1999.

Miller, P.I., Multispectral front maps for automatic detection of ocean colour features from SeaWiFS. International Journal of remote Sensing 25, 1437-1442, 2004.

Miller, P.I., Composite front maps for improved visibility of dynamic sea-surface features on cloudy SeaWiFS and AVHRR data, Journal of Marine Systems, 78, 327-336, 2009.

Muller, J.-P. and J. Fischer, The EU-CLOUDMAP project: Cirrus and contrail cloud-top maps from satellites for weather forecasting climate change analysis. Int. J. Remote Sensing, 28, 1915–1919, 2007.

Narita, H.: Specific surface of deposited snow II, Low Temp. Sci. A29, 69-81, 1971.

Neshyba, S., Grenfell, T. C., and Warren, S. G.: Representation of a nonspherical ice particle by a collection of independent spheres for scattering and absorption of radiation: II. Hexagonal columns and plates, J. Geophys. Res., 108, 4448, 2003.

Nolin, A. W., and Dozier, J., A hyperspectral method for remotely sensing the grain size of snow. Remote Sensing Environ., 74, 207–216, 2000.

Nolin, A. W., and S. Liang: Progress in bidirectional reflectance modeling and applications for surface particulate media: snow and soils, Remote Sens. Rev., 18, 307-342, 2000

Nolin, A.W. and Dozier, J., Estimating snow grain size using AVIRIS data. Remote Sensing Environ., 44, 231–238, 1993.

Painter, T.H., Roberts, D.A., Green, R.O. and Dozier, J. ,The effect of grain size on spectral mix-ture analysis of snow-covered area from AVIRIS data. *Remote Sensing of Environ.*, 65, pp. 320-332, 1998

Painter, T. H., Dozier, J., Roberts, D. A., Davis, R.E., and Greene, R.O.: Retrieval of subpixel snow-covered area and grain size from imaging spectrometer data, *Remote Sensing of Environment*, 85, 64–77, 2003

Painter, T.H., and J. Dozier, Measurements of the hemispherical – directional reflectance of snow at fine spectral and angular resolutions, *J. Geophys. Res.*, 109, doi: 10.1029/2003JD004458, 2004.

Painter T. H., Barrett, A. P., Landry, C. C., Neff, J. C., Cassidy, M. P., Lawrence, C. R., McBride, K. E., Farmer G. L., Impact of disturbed desert soils on duration of mountain snow cover, *Geophys. Res. Lett.*, 34, L12502, doi:10.1029/2007GL030284, 2007.

Paperin, M., Brockmann, C., 2007: ENVISAT Symposium Montreux (CH), 23-27 April 2007, Conference Proceedings 3P5.8: Atmospheric Properties from Optical/Infrared, Cloud Structures

Pawlowska, H., J.-L. Brenguier, Y. Fouquart, W. Armbruster, S. Bakan, J. Descloitres, J. Fischer, A. Fouilloux, J.-F. Gayet, S. Ghosh, P. Jonas, F. Parol, J. Pelon, L. Schüller, Microphysics/ radiation interaction in a stratocumulus cloud: The EUCREX mission 206 case study. *Atmos. Res.*, 55, 85-102, 2000.

Perla, R., Dozier, J., and Davis, R.E.: Preparation of serial sections in dry snow specimens. *J. Microsc.* 141, 111-114, 1986.

Phulpin T., Derrien M., and Brard A., A two dimensional histogram procedure to analyse cloud cover from NOAA satellite high resolution imagery. *J. Clim. Appl. Meteorol.* 22, 1332-1345, 1983.

Plummer et al, The GLOBCARBON Cloud Detection System for the Along-Track Scanning Radiometer (ATSR) Sensor Series, *IEEE TRANSACTIONS ON GEOSCIENCE AND REMOTE SENSING*, VOL. 46, NO. 6, JUNE 2008

Polar View, Service Description: <http://www.polarview.org/services/index.htm>, 2008

Preusker, R., Hühnerbein, A., Fischer, J., 2006, MERIS Global Land Surface Albedo Maps, ATBD Cloud Detection. <http://www.brockmann-consult.de/albedomap/pdf/MERIS-AlbedoMap-ATBD-CloudDetection1.0.pdf>

Prodex, Norway: EuroCryoClim Pilot Project Technical Proposal, [http://portal.opengeospatial.org/files/?artifact\\_id=30103](http://portal.opengeospatial.org/files/?artifact_id=30103), 2007



Rathke et al, Evaluation of four approximate methods for calculating infrared radiances in cloudy atmospheres, *Journal of Quantitative Spectroscopy & Radiative Transfer* 75 (2002) 297–321, 2002.

Rathke, C., J. Fischer, S. Neshyba, und M. Shupe, Improving IR cloud phase determination with 20 microns spectral observations, *Geophys. Res. Lett.*, 29 (8), 2002.

Rossow, W.B., and Schiffer, R.A., Advances in Understanding Clouds from ISCCP. *Bull. Amer. Meteor. Soc.*, 80, 2261-2288, 1999.

Sailsbury, J.W., D. M. D’Aria, A. Wald, Measurements of thermal infrared spectral reflectance of frost, snow, and ice, *J. Geophys. Res.*, 99, 24235-24240, 1994.

Salomonson, V.V. and Appel, I. ,Estimating fractional snow cover from MODIS using the nor-malized difference snow index.” *Remote Sensing of Environment*, Vol. 89, 2004, pp. 351-360, 2004.

Santer, R. et al, MERIS ATBD Pixel identification,  
[http://envisat.esa.int/instruments/meris/pdf/atbd\\_2\\_17.pdf](http://envisat.esa.int/instruments/meris/pdf/atbd_2_17.pdf), 1997.

Santer, R., V. Carrère V., P. Dubuisson P. and J.C. Roger, 1999. Atmospheric correction over land for MERIS, *International Journal of Remote Sensing*, 20 (9): 1819-1840.

Santer, R., and C. Schmechtig, 2000. Adjacency effects on water surfaces: primary scattering approximation and sensitivity study, *Applied Optics*, 39 (3): 361-375

Saunders R.W., and Kriebel K.T., An improved method for detecting clear sky and cloudy radiances from AVHRR data. *Int. J. Rem. Sens.* 9: 123-150, (1988)..

Schaaf, C. B., , et al., First operational BRDF, albedo and nadir reflectance products from MODIS, *Remote Sens. Env.*, 83, 135– 148., 2002.

Schiller et al, A METHOD FOR DETECTION AND CLASSIFICATION OF CLOUDS OVER WATER, MERIS - AATSR Workshop, 2008. ESRIN, Frascati, Italy; Workshop Proceedings, 2008.

Shi et al, Detection of daytime arctic clouds using MISR and MODIS, *Remote Sensing of Environment* 107 (2007) 172–184, 2007.

Simpson et al, Improved cloud detection for daytime AVHRR scenes over land, 1996.

Simpson et al, Improved Cloud Detection in Along Track Scanning Radiometer Data over the Ocean, *REMOTE SENS. ENVIRON.* 65:1–24, 1998.

Snyder, W.C., Z. Wan, Y. Zhang, Y.Z. Feng, Classification-based emissivity for land surface temperature measurement from space. *Int. J. Remote Sens.* :2753–74, 1998.

Solberg, Euroclim presentation at GlobSnow User Consultation meeting, [http://dup.esrin.esa.int/Files/News/2\\_Solberg.pdf](http://dup.esrin.esa.int/Files/News/2_Solberg.pdf) , Bern, 14.02.2008

Stamnes, K., Tsay, S. C., Wiscombe, W., and Jayaweera K., Numerically stable algorithm for discrete-ordinate method radiative transfer in multiple scattering and emitting layered media, *Appl. Optics*, 27, 2502-2510, 1988.

Stamnes, K., et al., 2007: [ADEOS-II/GLI snow/ice products — Part I: Scientific basis](#), *Remote Sensing of Environment*, 111, 258-273.

Steffen, K., Bidirectional reflectance of snow at 500-600nm. In *Large Scale Effects of Seasonal Snow Cover*, ed. by B. Goodison, R. G. Barry, J. Dozier, 436pp. IAHS Publication Series, 166: 415-425, 1987.

Stroeve, J.C., K. K. Steffen, Variability of AVHRR-derived clear-sky surface temperature over the Greenland ice sheet. *J. Appl. Meteorol.* 37:23–31, 1998

Stroeve et al., Accuracy assessment of the MODIS 16-day albedo product for snow: comparisons with Greenland in situ measurements, *Remote Sens. Env.*, 94, 46-60, 2005.

Susskind et al, Determination of ATM and surface parameters from simulated Air/AMS/HSB sounding data retrieval and clouds clearing methodology, *Adv. Space Rex Vol. 21, No. 3.* pp. 36%384,1998

Tanikawa et al., Monte Carlo simulations of spectral albedo of artificial snowpacks composed of spherical and nonspherical particles, *Appl. Optics*, 45, 5310-5319.

Tanikawa, T., Aoki, T., and Nishio, F., Remote sensing of snow grain-size and impurities from Airborne Multispectral Scanner data using a snow bidirectional reflectance distribution function model. *Annals Glaciol.*, 34, 74-80, 2002.

Tanikawa et al., Snow bidirectional reflectance model using nonspherical snow particles and its validation with field measurements, *EARSel Proceedings*, 5 137-145, 2006b.

Tanré, D., C. Deroo., P. Duhaut, M. Herman, J.J. Morcrette, J. Perbos and P.Y. Deschamps, 1990. Description of a computer code to simulate the satellite signal in the solar spectrum: 5S code, *International Journal of Remote Sensing*, 11: 659-668..

Tedesco, M., and Kokhanovsky A. A., The semi-analytical snow retrieval algorithm and its application to MODIS data, *Rem. Sens. Env.*, 110, 317-331, 2007.

Tedesco, M.: Special issue 'Remote Sensing of the Cryosphere' *Remote Sensing Environ.*, 111, 135, 2007.

Underwood, E.E.: *Quantitative stereology*, Addison-Wesley, Reading, MA, 1970.

Vermote, E., and Vermeulen, A., Atmospheric correction algorithm: Spectral reflectances (MOD09), ATBD version 4.0 available at [http://eosps0.gsfc.nasa.gov/ftp\\_ATBD/REVIEW/MODIS/ATBD-MOD-08/atbd-mod-08.pdf](http://eosps0.gsfc.nasa.gov/ftp_ATBD/REVIEW/MODIS/ATBD-MOD-08/atbd-mod-08.pdf), 1999.

Wald, AE., Modeling thermal infrared (2–14 m) reflectance spectra of frost and snow. *J. Geophys. Res. Solid Earth* :24241–50, 1994.

Wan ZM, Y. Zhang, MODIS UCSB Emissivity Library. <http://www.ices.ucsb.edu/modis/EMIS/html/em.html>, 1999.

Warren, S.G., and Wiscombe, W.J., A model for the spectral albedo of snow. II: Snow containing atmospheric aerosols. *J. Atmos. Sci.* 37, 2734-2733, 1980.

Warren, S. G., Optical properties of snow, *Rev. Geophys.*, 20, 67-89, 1982.

Warren, S. G., Optical constants of ice from the ultraviolet to the microwave. *Appl. Opt.*, 23, 1206-1225, 1984.

Warren, S.G., and Wiscombe, W.J.: Dirty snow after nuclear war. *Nature*, 313, 467-470, 1985.

Warren, S.G., Brandt, R.E., and Grenfell, T.C., Visible and near-ultraviolet absorption spectrum of ice from transmission of solar radiation into snow, *Applied Optics*, 45, 5320-5334, 2006.

Warren et al., Effects of surface roughness on bidirectional reflectance of Antarctic snow, *J. Geophys. Res.*, 103, 25789-25807., 1998.

Warren S. G., R. E. Brandt , Optical constants of ice from the ultraviolet to the microwave: A revised compilation, *J. Geophys. Res.*, 113, D14220, doi:10.1029/2007JD009744, 2008.

Wiscombe, W. J., The delta-Eddington approximation for a vertically inhomogeneous atmosphere, *NCAR Technical Note*, NCAR/TN-121+STR, 1-66, 1977.

Wiscombe, W. and Warren, S., A model for the spectral albedo of snow. 1: pure snow, *J. Atmos. Sci.*, 37, 2712-2733, 1980.

WMO, Second Report on the Adequacy of the Global Observing Systems for Climate in Support of the UNFCCC, GCOS-82, (WMO/TD No. 1143) and its Technical Annexes, April 2003

WMO, Systematic Observation Requirements for Satellite-based Products for Climate: Supplemental Details to the satellite-based component of the "Implementation Plan for the Global Observing System for Climate in support of the UNFCCC (GCOS-92)", GCOS-107, September 2006 (WMO/TD No.1338).

Wylie, D., 1998: Cirrus and Weather: A satellite perspective. OSA Meeting, pp.66-68, Baltimore, U.S.A., 6-8, Oct. 1998

Xie, Y., Yang, P., Gao, B.-C., Kattawar, G. W., Mishchenko M. I., Effect of ice crystal shape and effective size on snow bidirectional reflectance, *Journal of Quantitative Spectroscopy and Radiative Transfer*, 100, 457-469, 2006.

Zege, E. P., Ivanov A. P., and Katsev I. L., *Image transfer through a scattering medium*, Berlin: Springer, 1991.

Zhou, X., Li, S. and Stamnes, K., Effects of vertical inhomogeneity on snow spectral albedo and its implications for remote sensing of snow, *J. Geophys. Res.*, 108, 4738, 2003. doi: 10.1029/2003JD003859, 2003.

***End of Document***